

DIPLOMARBEIT

Investigation of the isotope effect in hydrogen-induced blistering of silicon using kinetic Monte Carlo simulation

ausgeführt zum Zwecke der Erlangung des akademischen Grades eines Diplom-Ingenieurs
unter der Leitung von

A.o.Univ.Prof. Dr. Gerhard Hobler
362
Institut für Festkörperelektronik

eingereicht an der Technischen Universität Wien
Fakultät für Elektrotechnik und Informationstechnik

von

Thomas Zahel
9825030
Klesheimstr.2, 2000 Stockerau

Wien, im Dezember 2004

Abstract

Silicon-on-insulator (SOI) structures were introduced in the 1960s and exhibit several advantages over bulk silicon material. Besides performance and economical aspects SOI is the material combination that could guarantee the survival of traditional silicon technology. Many different approaches to the manufacturing of this structure were proposed, involving deposition, wafer bonding and ion implantation. A commercially successful approach is the Smart Cut™ process which combines hydrogen implantation and wafer bonding. This process takes advantage of otherwise unwanted surface effects referred to as blistering and exfoliation, which appear due to extended defects caused by implantation. These defects are termed as hydrogen platelets and have been widely studied. Many physical aspects, however, are still unclear. E.g. an unexpected isotope effect of blistering in the low energy implantation region has been reported.

In this thesis a combination of binary collision simulation and kinetic Monte Carlo simulation is used to investigate the effects leading to the isotope effect. To accurately treat the simulation of hydrogen/deuterium implantation and the resulting defect distribution an extensive study of the literature was done. The experimental results and the theories about hydrogen platelets are summarized in a separate chapter. The simulation results agree with the experimental results and the theory about the isotope effect. In particular, it could be shown that hydrogen is bound preferably to monovacancies and deuterium is mostly bound to multivacancies after implantation at room temperature, corresponding to the experimental results. Further investigations revealed that this difference is due to the initial ratio of vacancies and hydrogen/deuterium atoms. Moreover, a simple model of this defect behavior is proposed.

The simulation results do not only confirm the assumptions about the isotope effect of blistering, but also lead to conclusions about the mechanism of platelet nucleation: VH_4 defects appear to be involved in the process of platelet nucleation, whereas no indication for the involvement of H_2^* defects could be found.

Contents

1	Introduction	7
2	Smart Cut™ process	11
2.1	Blistering and exfoliation	11
2.2	Process description	12
2.3	Process variations and applications	14
3	Exp. on low energy hydrogen implantation	17
3.1	Dose dependence of blistering	17
3.2	Isotope effect of blistering	20
4	Hydrogen in crystalline silicon	27
4.1	Hydrogen states and motion	27
4.2	Hydrogen-defect interaction	29
4.3	Platelets	30
4.3.1	Experimental data	30
4.3.2	Blistering and splitting kinetics	44
4.3.3	Platelet theories	47
4.3.4	Discussion of the isotope effect	54
5	Simulation	57
5.1	Goals for the sim. of hydrogen platelet nucleation and growth	57
5.2	Simulation methods and tools	58
5.2.1	IMSIL	59
5.2.2	Kinetic lattice Monte Carlo simulator (kLMC)	60
5.3	Setup of the simulation and simulation param.	64
6	Results	67
6.1	Initial damage and choice of simulation box	67
6.2	Defect evolution	67
6.3	Discussion	71
6.4	Conclusions	79
7	Outlook	81

Chapter 1

Introduction

In the mid 1960s silicon-on-insulator (SOI) structures were introduced because of their tolerance to radiation effects. A SOI structure consists of a single crystalline film which is separated from the bulk silicon by a SiO_2 layer [1].

Today, the motivation for developing SOI structures is mainly the performance aspect [1]. Circuits built in SOI technology exhibit several advantages over circuits built in traditional bulk silicon. Fig.1.1 shows cross sections of CMOS transistors built in bulk silicon and in SOI technology. SOI circuits (Fig.1.1(b)) consist of device islands, which are dielectrically isolated from the substrate and from each other. In contrary, the CMOS transistor shown in Fig.1.1(a) would not work in this configuration. An additional isolation between the adjacent components is essential. Such isolation can be achieved either by local oxidation (LOCOS) or by etching trenches into the silicon [2]. Circuits built in SOI have lower parasitic capacitances, which means that for a defined power consumption they are much faster than bulk silicon circuits. Moreover, the achievable density of circuits integrated on a wafer is higher. Concerning the processing it is obvious that building circuits in SOI is much simpler because steps for forming wells and etching trenches are not necessary.

Besides these performance and economical aspects, SOI materials could guarantee the survival of traditional silicon technology since SOI devices are more tolerant to the constraints of scaling-down rules [1]. The main problem of SOI fabrication is that the top silicon layer must be monocrystalline, whereas the separating SiO_2 film is amorphous. Many attempts have been made to achieve such a structure by deposition, but not many practical solutions have evolved. Only silicon-on-sapphire (SOS) has to be mentioned here [3].

Besides fabrication by layer deposition, attempts have been made by using ion implantation and wafer bonding. A possible approach is to directly implant a high dose of oxygen ($\sim 10^{18} \text{cm}^{-2}$) to produce SiO_2 in the silicon substrate. After annealing at high temperatures, the implanted oxygen forms a buried SiO_2 layer (BOX). This technology is referred to as "separation by implanted

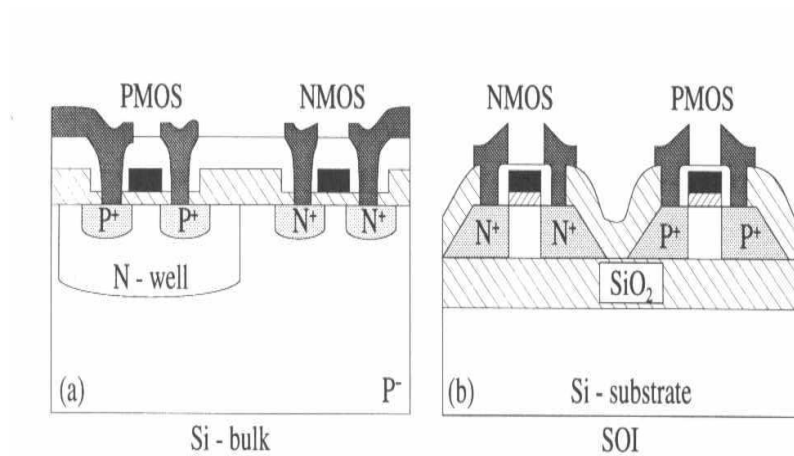


Figure 1.1: CMOS transistor built in (a) Si-bulk and (b) SOI technology (from [1])

oxygen” (SIMOX) [3].

For the purpose of wafer bonding the two wafers are cleaned in a RCA solution, followed by a water rinse. As a result the surface is covered with OH groups which makes it hydrophilic. After heating the wafer pair up to 1100°C it is held together by water bridges and water molecules [3].

A more or less brute force approach using wafer bonding is the ”bonded and etch-back” technology (BESOI). Two oxidized wafers are bonded together and annealed at high temperature to establish strong bonds comparable to the original wafer. One wafer is then etched back until a thin layer of silicon remains on the SiO_2 substrate [3].

A commercially successful approach to SOI wafer fabrication is the Smart Cut™ process. This process combines the methods of ion implantation and wafer bonding to achieve the splitting of a thin silicon layer. Hydrogen is implanted into an oxidized wafer (seed wafer), which is then bonded to a second wafer (handle wafer). During the heating step a layer from the seed wafer splits and forms the silicon layer on the oxide of the handle wafer. Finally, polishing makes the surface quality comparable to that of standard bulk silicon. The advantages are the control of the layer thickness by the implantation energy and the possibility to reuse the seed wafer. These SOI wafers are labeled as Unibond™ because of the fact that only $1+\epsilon$ ($\epsilon \ll 1$) starting wafers are needed to produce one SOI wafer [4].

Both Smart Cut™ and Unibond™ are trademarks of SOITEC. Starting in 1997 with 200mm Unibond™ wafers, a pilot line for 300mm wafers began in

2002. 300mm wafers are produced today in a large number. Moving from 130nm to 90nm to 65nm the silicon film of SOI wafers also has to scale down. Tab.1.1 shows the SOI roadmap from SOITEC [4].

Start in production	2002	2003	2004	2005	2006
Si layer thickness [Å]	1000	500-700	350-700	200-700	150-700
Si uniformity - all sites, all wafers, $\pm 3\sigma$ [Å]	± 75	± 50	± 30	± 20	± 10
AFM roughness RMS					
2x2 μm	1Å	1.5Å	2Å	2Å	2Å
10x10 μm	1.5Å	2.5Å	3.5Å	3Å	2.5Å
BOX layer thickness [Å]	1450	1450	1450	1000-1450	1000-1450
BOX layer TTV	$\pm 4\%$	$\pm 3\%$	$\pm 3\%$	$\pm 3\%$	$\pm 3\%$

Table 1.1: *SOITEC SOI roadmap (from [4])*

As it can be seen in Tab.1.1, requirements for SOI films will scale down dramatically in the next few years. Since the layer thickness is directly related to the implantation energy it is obvious that the implantation energy will have to decrease as well.

Although the Smart Cut™ process works well, several questions about the underlying physical aspects are still unsolved. Many experimental and theoretical investigations have been done in the last years, leading to partially contradicting results.

The Smart Cut™ process and the effects on which it is based are discussed in Chapter 2. Process variations and applications are reported. Chapter 3 describes the experiments on low energy implantation recently done by Moutanabbir *et al.* [5–7]. These experiments are related to the aspect of layer splitting and reveal a narrow fluence window and a significant isotope effect. The results of these investigations are described in detail, since the isotope effect is the main motivation for this thesis. In Chapter 4 a review of the role of hydrogen in silicon is given and defect structures directly connected to the Smart Cut™ process are discussed. Chapter 5 covers the simulation approach and the modelling done in this thesis. The results of the simulations are discussed in Chapter 6.

Chapter 2

Smart Cut™ process

The Smart Cut™ process takes advantage of blistering and exfoliation. These effects have been known in metals and semiconductors since the 1980s. In silicon, the implantation of a high dose of hydrogen leads to the formation of blisters at the silicon surface upon annealing. By increasing the dose these blisters can burst, resulting in the exfoliation of the blister surface area. This is by sure an unwanted effect of implantation, but by providing a mechanical stiffener M. Bruel [12] could increase the exfoliated area to the whole wafer size, a method which is now used under the term Smart Cut™. The process was originally invented for SOI wafers, but it is not restricted to silicon.

2.1 Blistering and exfoliation

Implanting a high dose of inert gas or hydrogen into materials can lead to surface effects like blistering, swelling, flaking and exfoliation [8]. Early reports on these effects were connected with radiation damage by helium and hydrogen and with studies of the implantation range of hydrogen and noble gases [9].

Bruel [10] reported that blistering and exfoliation of silicon surfaces could be obtained in two ways. One way is to keep the substrate in a temperature range of 25 to 300°C during implantation and use a high dose of hydrogen ions. Blistering becomes visible for a dose of $\sim 2 \times 10^{17} \text{cm}^{-2}$, flaking if the dose is further increased. The second possibility has to be done in two steps. At first, a dose of $3\text{-}5 \times 10^{16} \text{cm}^{-2}$ is implanted, while the substrate temperature is kept in the 25 to 300°C range. At this point no altering of the surface can be observed. After a thermal treatment in the range of 400-600°C blistering and flaking occurs.

Fig.2.1 shows an optical microscopy image of a silicon sample implanted with $1 \times 10^{17} \text{H/cm}^2$ and annealed to 475°C. "Popped" blisters with a size between 10 and 250nm and "capped" bubbles with a size of 10-70nm are clearly visible. An

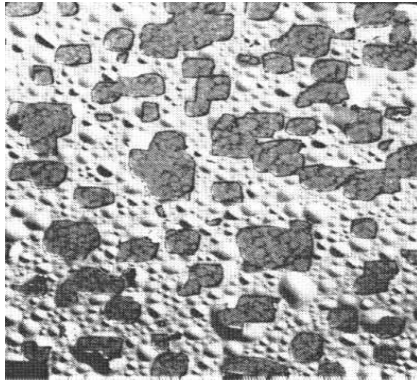


Figure 2.1: *Optical microscopy image of silicon implanted to a dose of $1 \times 10^{17} \text{H/cm}^2$ and annealing to 475°C (from [11])*

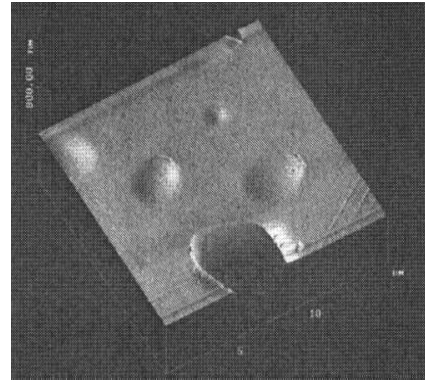


Figure 2.2: *AFM image of the sample shown in 2.1 (from [11])*

atomic force microscopy (AFM) view of the same sample is shown in Fig.2.2. The measured depth of the craters formed by blistering is found to be equal to the peak of the hydrogen implantation profile [11].

2.2 Process description

Bruel investigated the possibility of extending the size of flakes to wafer size in order to achieve a new technology for SOI materials. The process was developed under the name "IMPROVE" (IMplantation of PROtons Voids Engineering) and is now referred to as Smart Cut™ [10][12].

The technology combines ion implantation, most commonly of hydrogen, and wafer bonding, resulting in the splitting of a thin layer from the wafer. Bruel used a second wafer as a stiffener to redirect the pressure leading to blistering into the lateral direction, creating a weakened plane. This plane either splits during heat treatment, or can be cleaved by applying stress [9].

Figure 2.3 shows the basic Smart Cut™ process flow which includes the following steps [10][12].

- Implantation of hydrogen into a wafer with a dielectric layer (seed wafer), for example SiO_2 , which becomes the buried oxide.
- Hydrophilic bonding to a second wafer (handle wafer) at room temperature. Both wafers are cleaned by using a modified RCA process before bonding
- During the heat treatment at $400\text{-}600^\circ\text{C}$ the implanted wafer splits which results in a thin layer of monocrystalline silicon on the oxide layer of the

handle wafer.

- Further heat treatment at temperatures $>1000^{\circ}\text{C}$ strengthens the chemical bonds
- After splitting, the silicon surface has to be chemico-mechanically polished

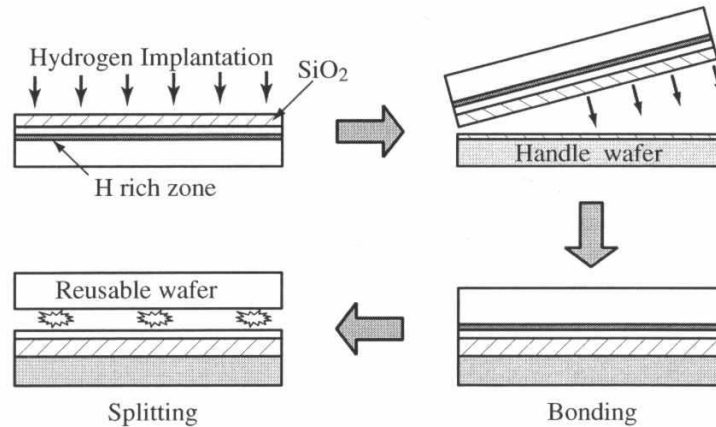


Figure 2.3: *Smart Cut™* process steps (from [9])

The process has several advantages over other technologies used for the fabrication of SOI structures [13].

- Implantation enables a high uniformity of the top silicon layer and wafer bonding preserves the good quality of the bulk silicon
- The buried oxide layer is thermally grown and the thickness can be adjusted with high reliability
- The total thickness of the silicon layer is directly related to the ion energy (8nm/keV in silicon)
- All the technology steps can be performed with standard equipment
- Only one bulk wafer is required per SOI wafer

Today, implantation energies are typically between 20 and 200keV [14]. SOI wafers obtained by Smart Cut™ have a silicon layer homogeneity of better than $\pm 5\text{nm}$ over a 200mm wafer. The process was previously developed for 0.1-0.2 μm silicon layers on top of 0.1-0.2 μm buried oxide, whereas future trends target on a layer thickness of a few tens of nanometers.

The micro-roughness of an as-finished SOI wafer ($\sim 1\text{\AA}$ over $1 \times 1 \mu\text{m}^2$) is comparable to that of silicon bulk wafers [15]. Fig.2.4 shows the transmission electron microscopy (TEM) image of a SOI structure obtained by Smart Cut™.

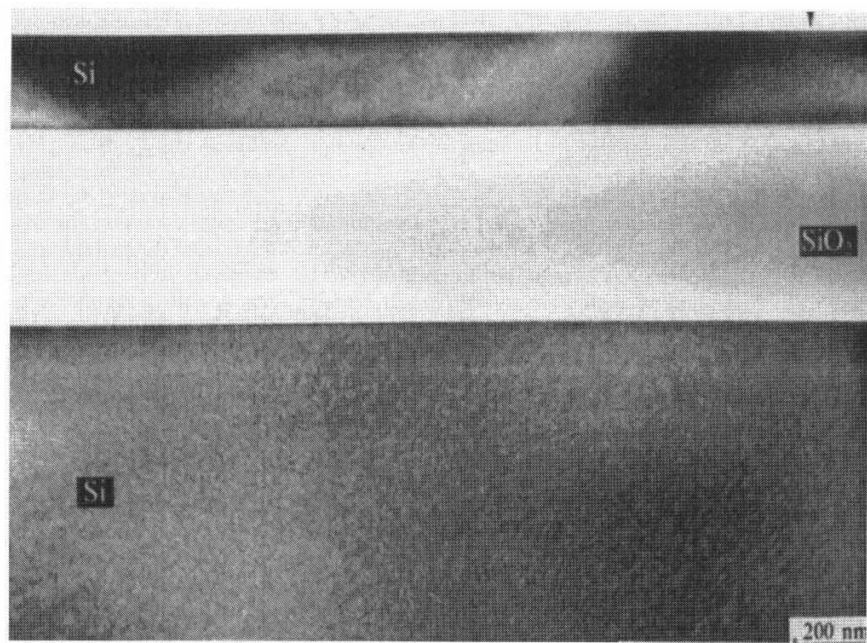


Figure 2.4: TEM of a SOI structure obtained by smart-cut (from [13])

2.3 Process variations and applications

Transfer of thin films can also be achieved with other gases, like helium and other noble gases. A co-implantation of first hydrogen and then helium leads to layer splitting at a dose of $7.5 \times 10^{15} \text{H/cm}^2$ and 10^{16}He/cm^2 , whereas $2 \times 10^{17} \text{He/cm}^2$ and $6 \times 10^{16} \text{H/cm}^2$ would be needed if implanted alone under the same conditions [16].

The heating time and temperature requirements can be reduced if the wafer is first doped with boron. This can be useful for transferring silicon layers onto materials with a very different thermal expansion coefficient [17].

Although the Smart Cut™ process was originally developed to manufacture SOI, it is a generic layer transfer technology. The process enables the transfer of any monocrystalline film on any substrate, which fulfills the following conditions [13]:

- Ability to generate blisters after implantation of protons or inert gas ions
- Possibility of bonding the implanted wafer to a handle wafer with sufficient bonding energy to prevent de-bonding during heating

- Existence of a sufficiently low splitting temperature

So far, material combinations obtained by layer splitting include silicon on quartz (SOQ), single crystalline films on plastic, germanium on insulator [18], silicon-carbide on insulator [19], GaAs on silicon [20] and InP on insulator [21]. The concept of introducing strain of the silicon lattice to enhance the electron mobility can also be applied to SOI [4]. Besides producing structures on insulators it is possible to produce a contact layer using the Smart Cut™ process. The hydrogen bonding is in this case replaced by metallic bonding to achieve thin films of Si, GaAs or InP on silicon substrates [22]. The process is not limited to the transfer of a single layer. By repeating the process a multiple SOI stack structure can be achieved [23]. Integrated circuits can be transferred as a film from the original substrate to a different substrate which could be used for thin film transistors on glass or quartz [24].

Chapter 3

Experiments on low energy hydrogen implantation

3.1 Dose dependence of blistering

Recently experiments on low energy hydrogen implantation and the blistering effect connected to it have been done by Moutanabbir *et al.* [5–7]. Undoped silicon wafers were implanted with 2, 5 or 10 keV hydrogen or deuterium ions at a fluence of 1×10^{16} to $1 \times 10^{17} \text{cm}^{-2}$ at room temperature and annealed for ~ 50 s at temperatures up to 650°C . In the course of annealing the partial pressure of H_2 , D_2 and HD was monitored by a mass spectrometer. The surface topography of the samples was then analyzed by atomic force microscopy (AFM). To reveal the defect structure additional investigations involved Raman scattering spectroscopy [7].

Fig.3.1 shows the AFM micrographs of the silicon surface for hydrogen implantation at 5keV for different fluences after annealing, which reveal an unexpected dose effect. A fluence of $2 \times 10^{16} \text{H}/\text{cm}^2$ leads to dome shaped blisters of a very high density with diameters of $\sim 700 \text{nm}$ and heights of 10-20nm. Less blistering can be observed for a fluence of $4 \times 10^{16} \text{H}/\text{cm}^2$. Some blisters are completely exfoliated, inducing craters of $\sim 90 \text{nm}$ depth with a top diameter of $\sim 800 \text{nm}$. Increasing the dose to $6 \times 10^{16} \text{H}/\text{cm}^2$ leads to the disappearance of blistering. The surface is only very rough. This narrow fluence window of blistering can be seen in Fig.3.2 and could also be observed for implantations at 2keV and 10keV (Fig.3.3) [5].

An indication for the effect of blister absence can be seen in the thermal desorption spectra (TDS) (Fig.3.4). The H_2 spectrum corresponding to a fluence of $2 \times 10^{16} \text{H}/\text{cm}^2$ shows a wide peak centered at around 400°C and gas losses starting at 200°C . For the high fluence of $6 \times 10^{16} \text{H}/\text{cm}^2$ no H_2 outdiffusion takes place for $T < 400^\circ\text{C}$, followed by slow desorption up to high temperatures. The

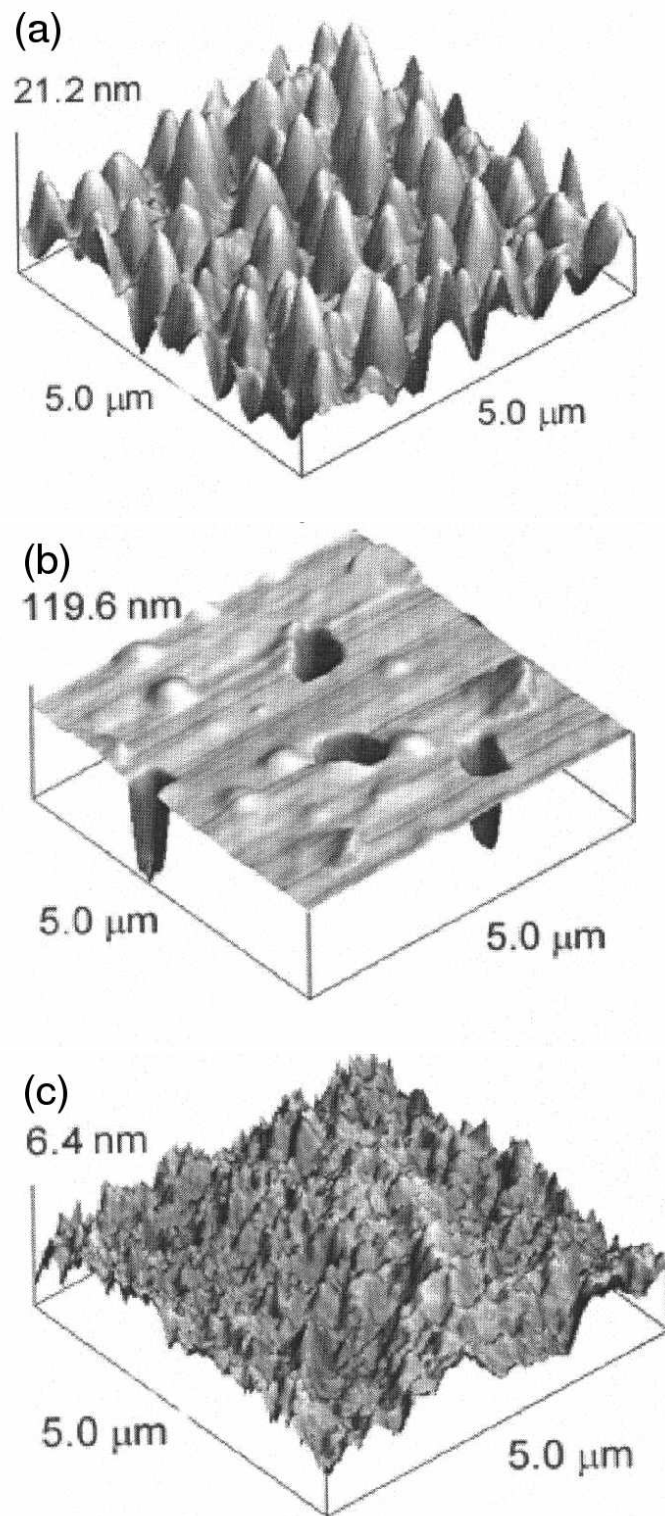


Figure 3.1: AFM images of silicon surfaces implanted with 5keV hydrogen and annealing up to 650°C (a) $2 \times 10^{16} \text{cm}^{-2}$ (b) $4 \times 10^{16} \text{cm}^{-2}$ (c) $6 \times 10^{16} \text{cm}^{-2}$ (from [5])

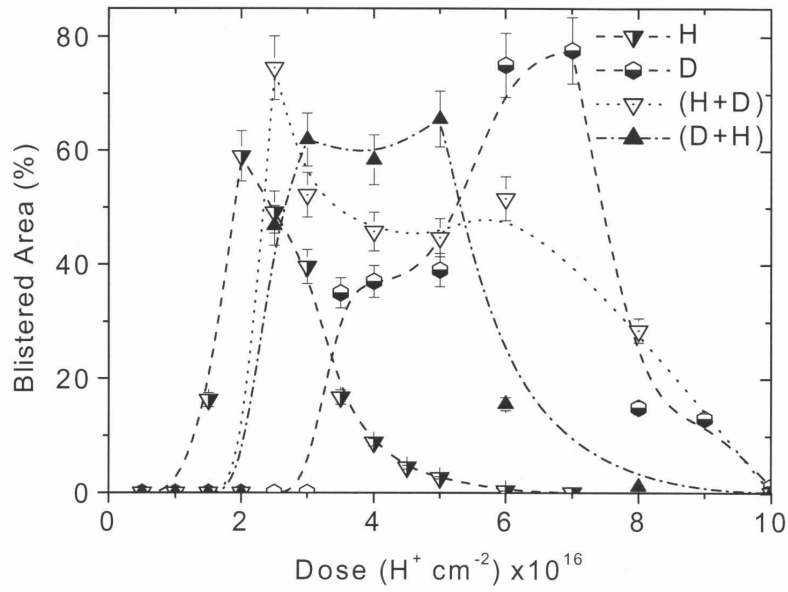


Figure 3.2: Blister-covered area as a function of total fluence of H and/or D implanted at 5keV (from [6])

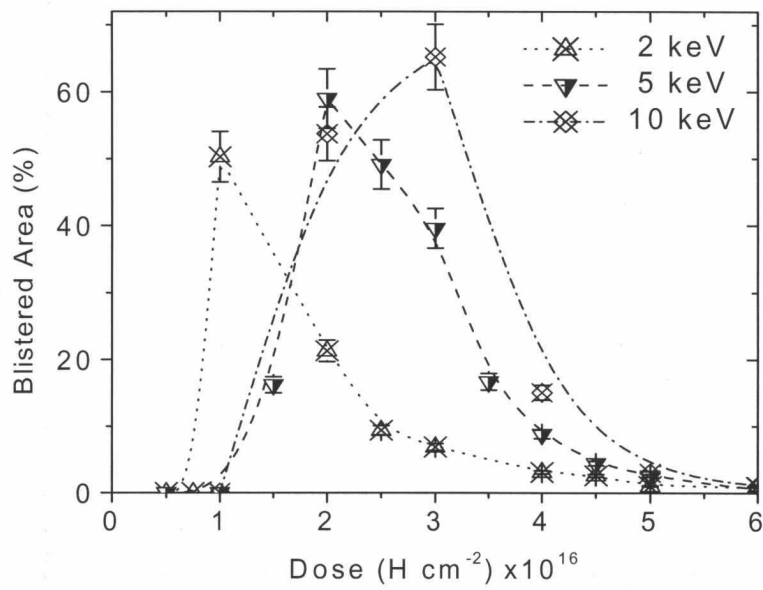


Figure 3.3: Blister-covered area as a function of H fluence at 2, 5, and 10keV (from [6])

absence of blistering may therefore be the result of missing H₂ in the 250-400°C temperature range.

3.2 Isotope effect of blistering

Fig.3.2 shows the blister-covered area as a function of the total fluence of H and/or D, implanted alone and combined. Implantation of deuterium also shows an unexpected isotope effect. Blistering cannot be observed below a fluency of $3.5 \times 10^{16} \text{H/cm}^2$. Disappearance takes place at a fluence of $8 \times 10^{16} \text{H/cm}^2$.

Since deuterium implantation produces more damage than hydrogen implantation, one would expect that blistering can be achieved more easily with deuterium, in contrast to the experimental results.

Blisters produced by deuterium implantation are larger (~80% of the surface), having twice the average volume of hydrogen blisters [5].

Blistering at low energy requires a lower dose than at high energy, but makes good control of it necessary. The blisters are rather small and flat with low internal pressure. The diameter of the blisters increases slowly with the implantation energy, covering wider areas of the surface, as can be seen in Fig.3.3 [6].

Fig.3.5 shows H₂ and D₂ spectra obtained by thermal desorption spectroscopy from samples implanted to $2 \times 10^{16} \text{H/cm}^2$. The H₂ spectrum shows a wide peak centered around 400°C and gas losses starting at 200°C. In contrast to this the D₂ spectrum has a small peak at 325°C which may be associated with gas outdiffusion from unstable defects and an asymmetric peak around 475°C. Moutanabbir *et al.* conclude from TDS data that D is more stable in silicon during annealing than H.

Fig.3.6 shows the Raman scattering spectroscopy results for hydrogen and deuterium implantation at 5keV to a dose of $2 \times 10^{16} \text{H/cm}^2$ at room temperature. It can be seen that the Raman intensity of the "low-frequency" broadband (LF), which is assumed to be mostly due to monohydride-terminated multivacancies ($V_n H_m$, $m \leq n$) and the Raman intensity of the "high-frequency" (HF) broadband, which is assumed to be mostly due to multihydride-terminated monovacancies (VH_m) are nearly equal in the case of hydrogen implantation. In the case of deuterium implantation the Raman intensity of the HF broadband is significantly lower than that of the LF broadband which leads Moutanabbir *et al.* to the conclusion that the isotope effect results from the different binding behavior of hydrogen and deuterium to vacancies.

Upon annealing it can be observed that there is a large loss of the LF broadband above 200°C and a relative stability of the HF broadband between 300°C and 400°C in the case of the hydrogen implantation (Fig.3.7). Additionally it can be seen, that there is an emergence of sharp spectral features. Whereas in the case of deuterium implantation (Fig.3.8), where no blistering takes place, the HF and the LF modes progressively disappear upon annealing. In comparison,

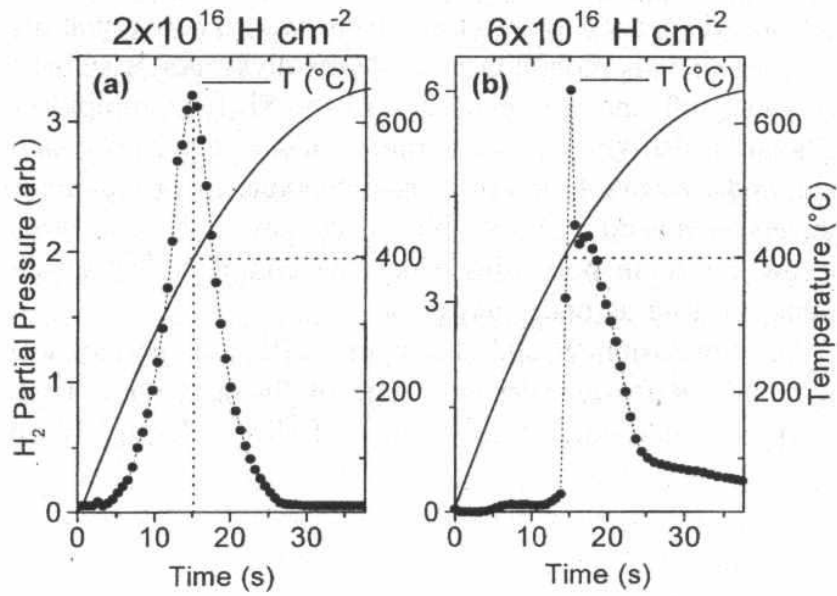


Figure 3.4: Hydrogen thermal desorption spectra of Si implanted at 5keV with (a) $2 \times 10^{16} \text{ cm}^{-2}$ (b) $6 \times 10^{16} \text{ cm}^{-2}$ (from [6])

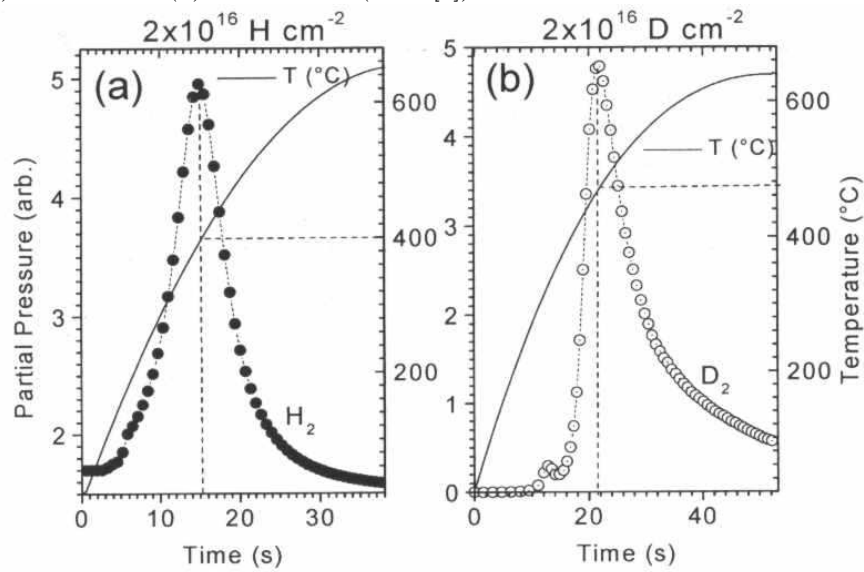


Figure 3.5: Thermal desorption spectra of Si implanted at 5keV with (a) $2 \times 10^{16} \text{ H cm}^{-2}$ (b) $2 \times 10^{16} \text{ D cm}^{-2}$ (from [5])

the spectra of the annealing of deuterium implanted to a dose of $6 \times 10^{16} \text{cm}^{-2}$, where blistering can be observed, show the appearance of sharp spectral features as in the case of hydrogen implantation (Fig.3.9). Therefore it can be expected that these modes are related to the formation of hydrogen platelets. The theories about the isotope effect will be discussed in Chapter 4.3.6.

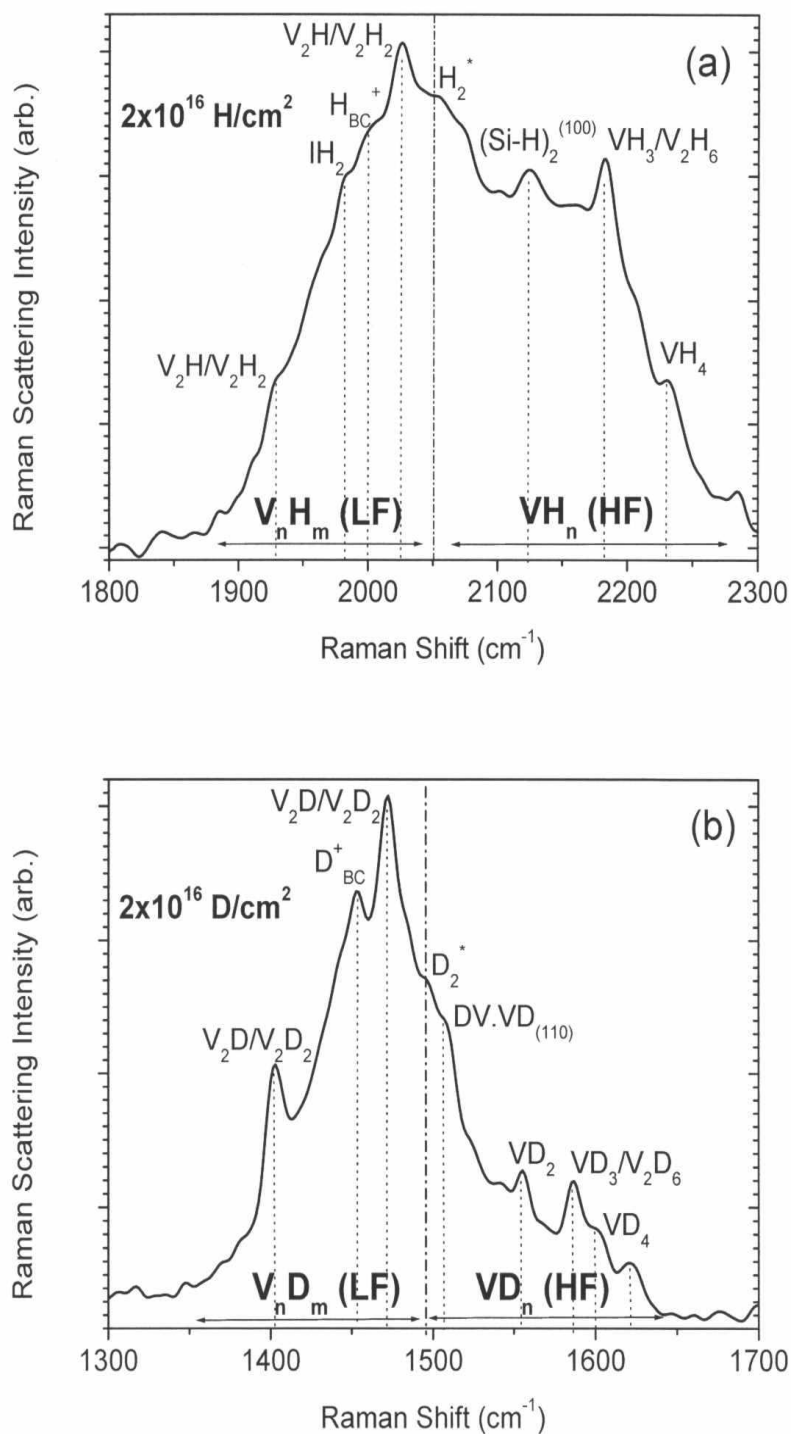


Figure 3.6: Si-H/D stretch mode regions of the Raman Scattering spectra obtained after implantation with $2 \times 10^{16} \text{ cm}^{-2}$ (a) H implantation (b) D implantation (from [7])

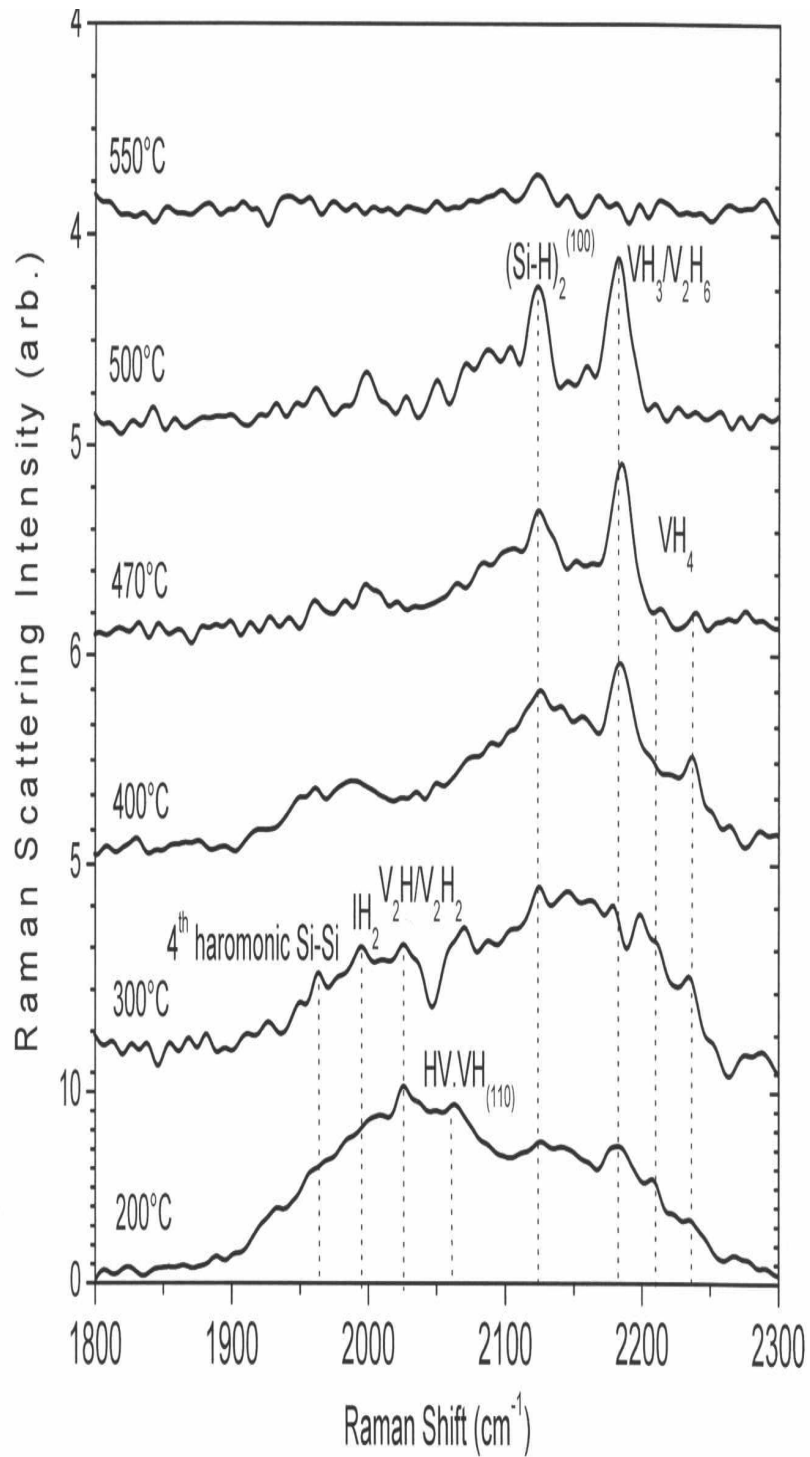


Figure 3.7: Temperature evolution of the Si-H stretch modes of Si implanted with $2 \times 10^{16} \text{Hcm}^{-2}$ (from [7])

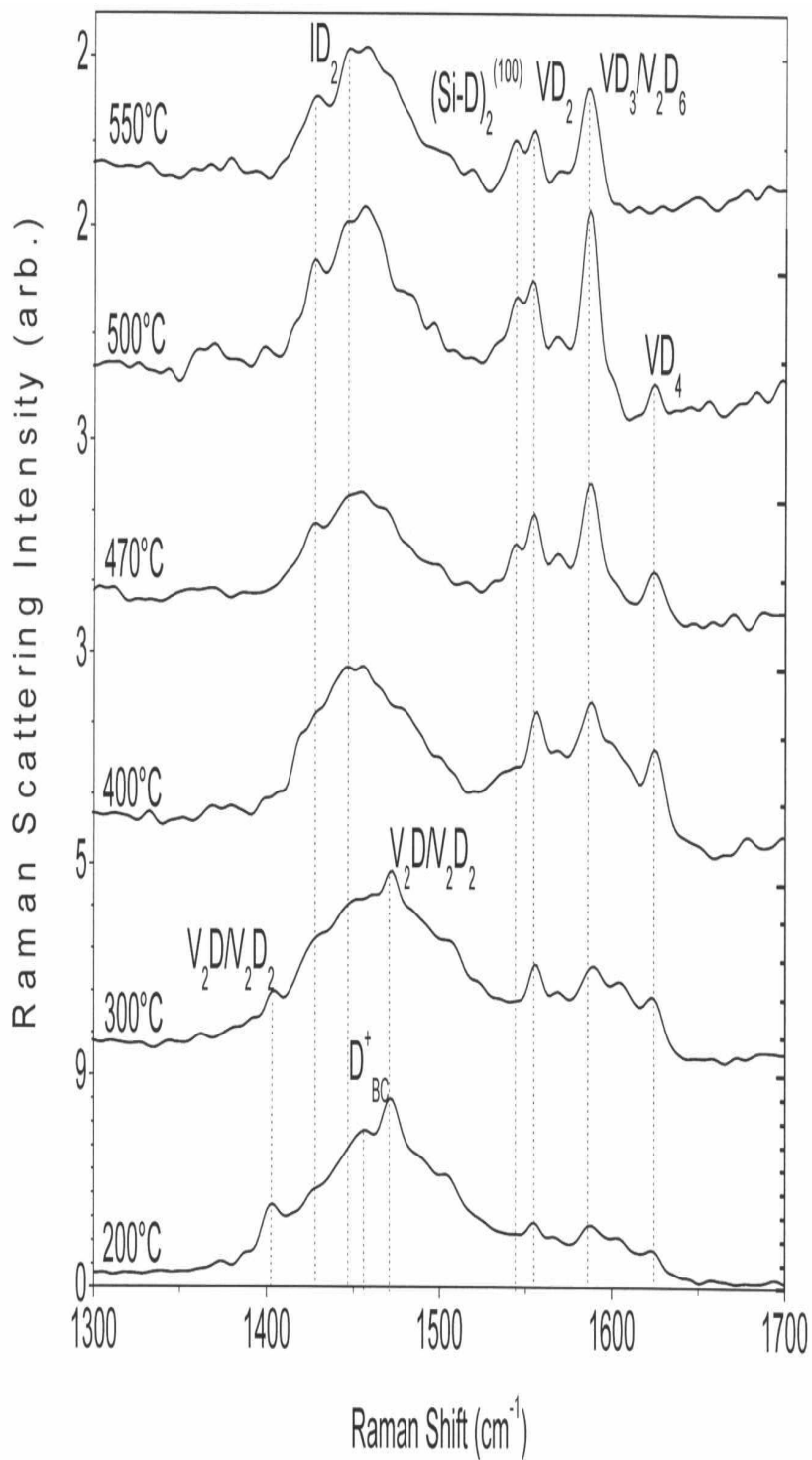


Figure 3.8: Temperature evolution of the Si-H stretch modes of Si implanted with $2 \times 10^{16} \text{ D cm}^{-2}$ (from [7])

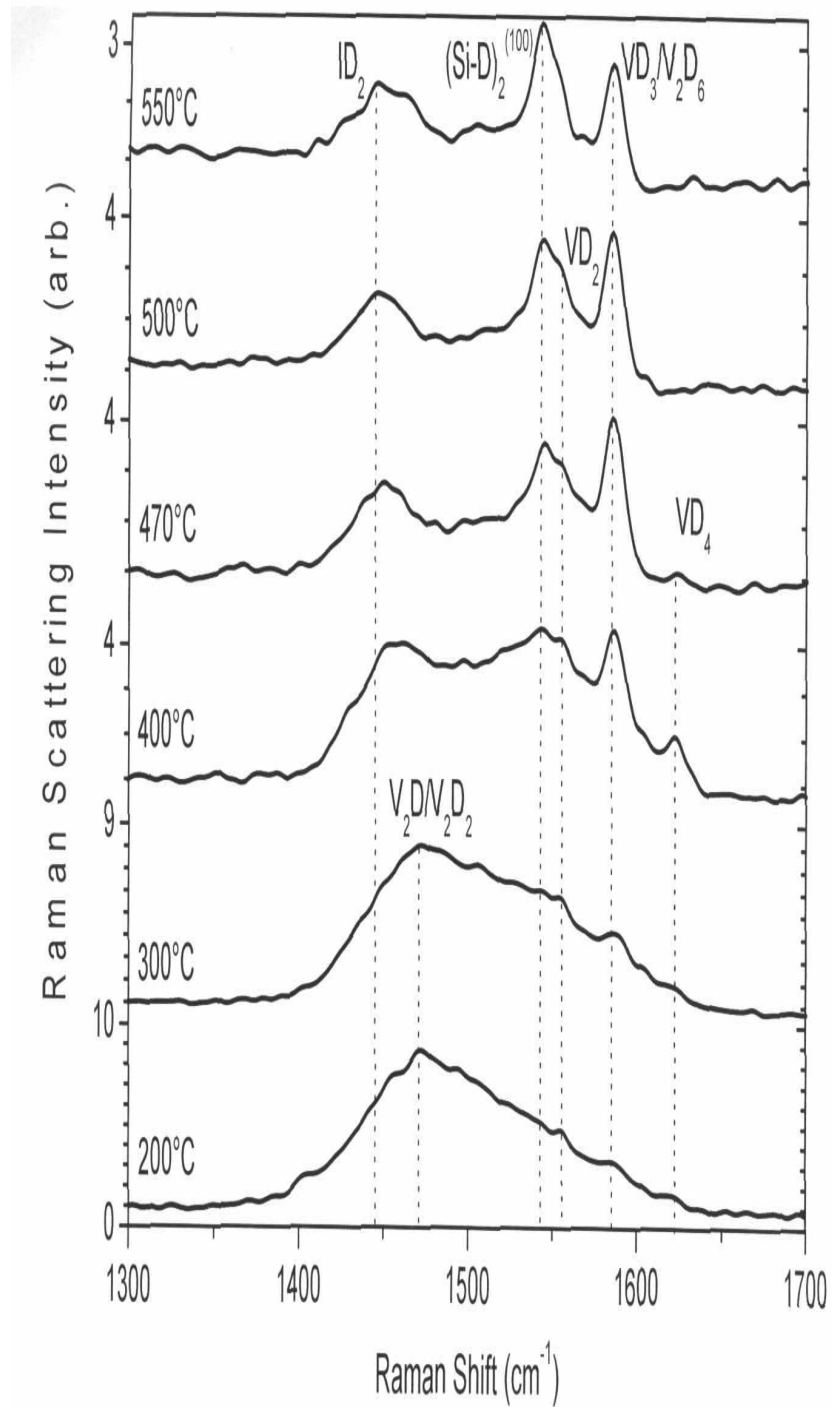


Figure 3.9: Temperature evolution of the Si-H stretch modes of Si implanted with $6 \times 10^{16} \text{ D cm}^{-2}$ (from [7])

Chapter 4

Hydrogen in crystalline silicon

Hydrogen in silicon exists in various configurations and charge states. It interacts with impurities and defects and is involved in the formation of extended defects, called hydrogen platelets, which are the cause for effects like blistering and exfoliation. The behavior of hydrogen is therefore of enormous interest for the understanding of these phenomena. The important issues are the states of hydrogen in silicon, their stability and mobility. Moreover, the experimental detection is also of great importance to reveal the defect nature of hydrogen platelets. This chapter tries to give a brief overview of the work done so far and the remaining problems are discussed. Based on this information hydrogen platelets are treated from the experimental and theoretical point of view and theories based on experiments and calculations are discussed. Finally, the possible reasons for the isotope effect presented in Chapter 3 are reported.

4.1 Hydrogen states and motion

In defect and impurity free silicon hydrogen exists in at least four different configurations. Isolated hydrogen atoms maybe at relaxed bond-centered (BC) sites, or at (or near) a tetrahedral interstitial (T) sites. Two atoms either form a molecule at the T site or a "bond-centered-antibonding" complex. These configurations are denoted as H_{BC} , H_T , H_2^T and H_2^* . Moreover, the isolated BC species can be found in the 0 and +1 charge states, the hydrogen atom at the T site in the 0 or -1 charge state [25].

The energies of various configurations of hydrogen were reported by Van de Walle [26] and Estreicher *et al.* [25]. Energy levels of isolated hydrogen in silicon were calculated by Herring *et al.* [27]. The relative stability of charge states of hydrogen were investigated by Deak *et al.* [28].

The important issue of hydrogen diffusion in silicon has been widely studied [29–35]. The diffusion of hydrogen can be described as a function of temperature, but not as usual through an Arrhenius law e^{-E_a/k_bT} . At lower temperatures, the trapping of hydrogen at vacancies may occur, resulting in trap-limited diffusion. Moreover, the diffusivity also depends on the state of hydrogen. Therefore, it is difficult to measure the diffusion coefficient, except at high temperature, where trapping does not occur [25]. Diffusion barriers for various diffusion paths can be found in [29]. The values vary between 0.43eV and 1.33eV. A calculation of the hydrogen diffusion coefficient was reported by Bedard *et al.* [35].

Although the interstitial H_2 molecule was suggested to play an important role in the diffusion of hydrogen and in hydrogen related defect reactions it could not be directly observed in silicon, until a few years ago the vibrational lines of H_2 , HD and D_2 were found [36]. The hydrogen molecule in silicon has been extensively studied theoretically [37–40] and experimentally [41–43]. A summary of the theoretical predictions of H_2 can be found in [44]. Despite this large number of investigations Stavola *et al.* [45] report, that there are still unsolved problems.

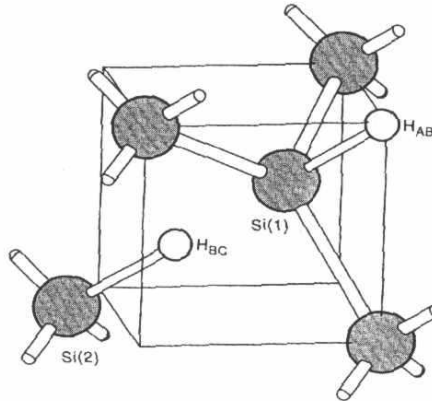


Figure 4.1: H_2^* defect (from [49])

The H_2^* defect was first proposed by Chang and Chadi [46, 47]. The defect consists of two hydrogen atoms which do not form a molecule. One atom is located at the bond-center (BC), the other atom is located at the anti-bonding (AB) position (see Fig.4.1). Chang and Chadi calculated the total energy of the complex and found it to be ~ 1.2 eV lower than that of two isolated, but 0.4eV higher in energy than the hydrogen molecule in its lowest energy configuration. Calculations of the diffusion barriers lead Chang and Chadi to the conclusion, that the H_2^* defect should be an important source for hydrogen diffusion, particularly at high hydrogen concentrations and at low temperatures. A diffusion

path was proposed, but it is not clear, whether this diffusion includes dissociation of the H_2^* defect or not.

An experimental study of the migration of the H_2^* complex was done by Johnson and Herring [48]. A migration energy was obtained, but this may either represent the diffusion of the complex as a unit, or the migration energy of the monoatomic species and half of the dissociation energy. Detailed infrared studies of the H_2^* complex were presented by Holbech *et al.* [49].

Estreicher *et al.* [50] point out that H_2 and H_2^* have never been observed to coexist and present the reactions for the conversion of H_2 into H_2^* . Both vacancies and interstitials dissociate the hydrogen molecule



Arrival of either an interstitial or a vacancy leads to the formation of H_2^*

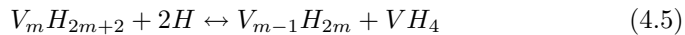


4.2 Hydrogen-defect interaction

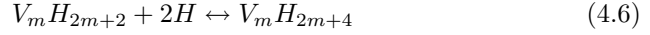
Several theoretical [51, 52] and experimental [53–56] investigations of the vibrational properties of hydrogen related defects were carried out, but the assignment of spectral features to defect types is still discussed.

The configurations, electronic structures and binding energies of hydrogen to small vacancy clusters were calculated by Estreicher *et al.* [57]. Possible energy gains ΔE by trapping hydrogen at vacancy-clusters $V_n + H_{BC} \rightarrow V_nH + \Delta E$ are in the order of 3.0 to 3.5eV, where the smallest gain is assigned to the smallest aggregate. The energies are all relative to bond-centered hydrogen in a perfect crystal. The energy comes mostly from the formation of strong Si-H bonds, but some energy is gained by relaxation of the vacancy aggregate. Larger aggregates can reconstruct more efficiently after hydrogen trapping which explains the higher energy gain.

Zhang and Branz [58] proposed that fully hydrogen passivated multivacancies can capture additional hydrogen at electrically inactive sites. First principle calculations show that splitting a multivacancy V_m with $m \geq 2$ into a monovacancy and a multivacancy V_{m-1} provides a low-strain pairing site for hydrogen lower than any bulk silicon pairing site. The capture of two additional hydrogen atoms by an hydrogen saturated multivacancy is accompanied by the ejection of a monovacancy through



In the case of a V_2H_6 defect the divacancy splits into two second nearest neighbor VH_4 defects. An alternative reaction without the ejection of a monovacancy leading to a higher binding energy is:



The binding energy of isolated hydrogen bound to an interstitial was calculated by Gharaibeh *et al.* [59]. The energy gain ΔE from $IH_{n-1} + H_{BC} \rightarrow IH_n + \Delta E$ was calculated for all possible configurations. Results show, that the most stable complex is the IH_2 complex, followed by IH_1 , IH_3 and IH_4 .

So far, little information can be found in the literature concerning the mobility of hydrogen saturated point defects. Saponi *et al.* [60] suggest that the only mobile VH_m defect could be the VH_1 defect. This diffusion mechanism starts with the motion of a silicon atom towards a vacancy, which moves along a curved path in the presence of a hydrogen atom. Next, a Si-H bond must be broken since that hydrogen atom forms a new bond with the silicon atom that was moving towards the vacancy. The final step includes rotation of the complex to recover the configuration of the VH_1 defect.

4.3 Platelets

Effects like blistering and exfoliation of the surface of hydrogen implanted wafers appear to be caused by extended defects induced by the implantation. These defects grow during annealing through the mechanism of a conservative Ostwald ripening process. It is assumed, that molecular hydrogen agglomerates in these cavities, which builds up the pressure necessary for the occurrence of the effects mentioned above. Experimental and theoretical investigations try to answer the following questions:

- Where are the defects located?
- What is the relation between platelet distribution and the hydrogen/damage profile?
- From which defects do the platelets nucleate?
- Which defect transformations take place during the growth of platelets?
- What are the reasons for the pressure which leads to blistering or exfoliation?
- Where does the splitting take place?

4.3.1 Experimental data

Johnson *et al.* [61] reported microdefects and electronic deep levels in silicon induced by hydrogenation. These defects visible on TEM views are unrelated

to either plasma or radiation damage and are described as hydrogen-stabilized platelets or microcracks. Secondary ion mass spectroscopy shows that platelets, which are predominantly oriented in the (111) plane correspond to a high concentration of hydrogen or deuterium. These platelets are not due to dislocations, since there is no indication for a net displacement in the lattice. Also the typical contrast for stacking faults (interstitial or vacancy loops) could not be observed. The platelets appear to be microcracks (diameter 3 to 12nm), where the separation between the atomic planes is increased by a slight displacement of silicon atoms. Investigation using Raman spectroscopy reveals that the platelets consist of Si-H bonds. Fig.4.2 shows the TEM view of a platelet distribution after hydrogen implantation before annealing.

Aspar *et al.* [8] observed platelets after implanting hydrogen. Most of the platelets lie in the (100) plane, only a few in the (111) plane. These platelets, which are also referred to as cavities, have a size around 10nm and all have the same thickness of 1nm. The cavities are restricted to the mean ion range of hydrogen R_p .

It seems that in the case of hydrogenated plasma treatment platelets in the (111) plane are favored, while platelets in the (100) plane are dominant in the case of hydrogen implantation [76].

On annealing at 500°C Aspar *et al.* [8] reported that (100) platelets grow in size, remain around R_p and do not move. To deduce the thermal evolution of the platelets, samples were implanted with 60% of the dose required for blistering and a cross-section transmission microscopy (XTEM) analysis was done for annealing at 500°C for various times. It was observed that although platelets exist before annealing they dramatically grow in size and density after 5min of annealing. For longer annealing the size still increases, but the density is reduced, while the number of hydrogen atoms involved stays constant. Aspar *et al.* conclude that this fact has two important meanings. First, there are no other sources or sinks for hydrogen than cavities, which means that the system can be seen as a closed box. Secondly, it means that all the initial hydrogen can be found in the cavities. Any hydrogen atom lost by one cavity is captured by another. This process must therefore involve hydrogen diffusion between the cavities in such a way that larger ones can grow at the expense of smaller ones. This mechanism can be described by the Ostwald ripening theory. Since the same study carried out for platelets lying in the (111) plane did not show any growth, Aspar *et al.* conclude that these platelets do not play a significant role in splitting.

A similar investigation of the annealing of a hydrogen implanted sample was done by Grisolia *et al.* [62]. Samples were annealed at 450°C for various times and the platelet evolution studied by XTEM. In contradiction to Aspar *et al.* [8] Grisolia *et al.* report that the platelets have reached their maximum density immediately after implantation (Fig.4.3). The density decreases upon further annealing and the hydrogen concentration stays constant in agreement with the results from Aspar *et al.*

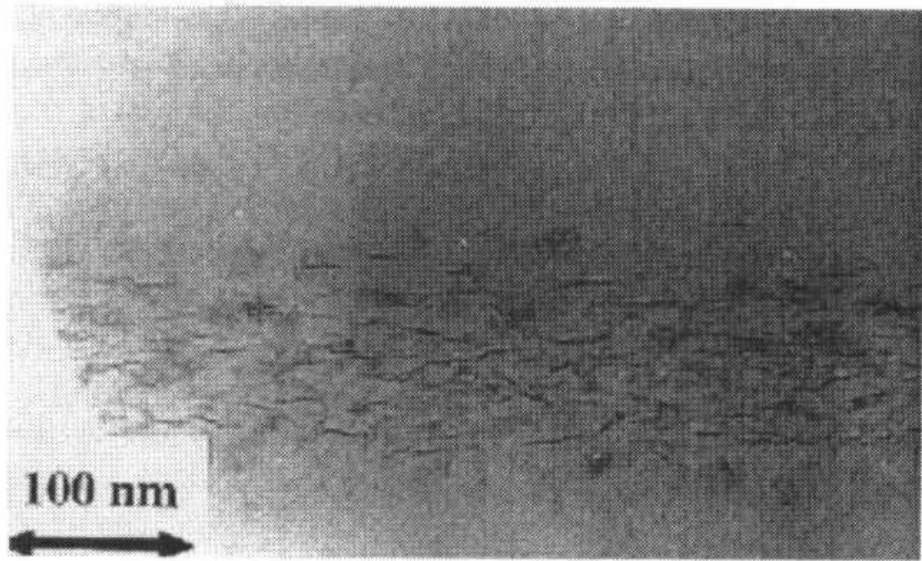


Figure 4.2: TEM view of a microcrack distribution after hydrogen implantation at room temperature (from [9])

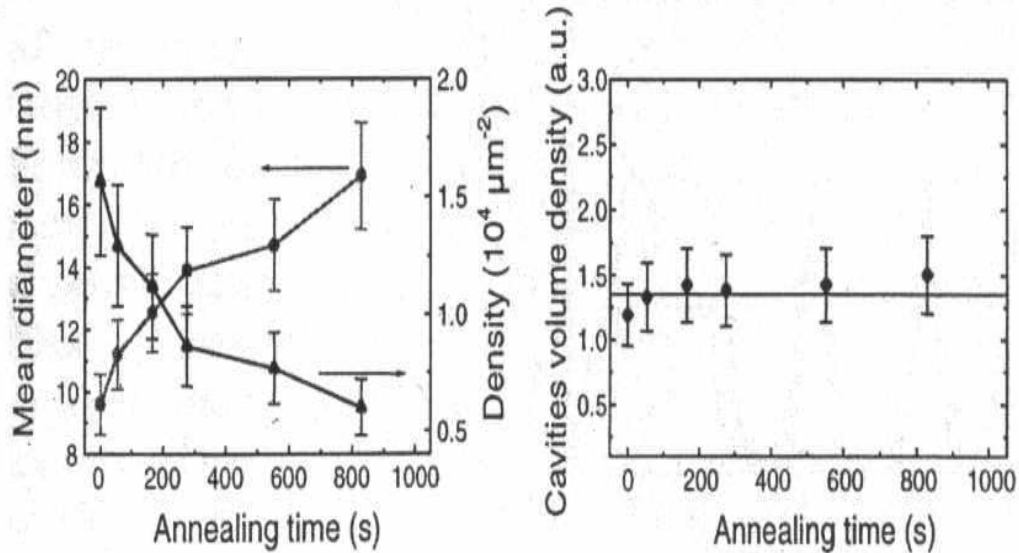


Figure 4.3: Evolution of the mean diameter, the density and the average volume of platelets (from [62])

A TEM study of an as-implanted sample annealed at 450°C done by Weldon *et al.* [11] reveals a connected network of microcracks forming a macrocrack ($2\text{-}3\mu\text{m}$ in length) parallel to the (100) plane. The crack predominantly consists of (100) planes connected by a minority of (111) planes. Fig.4.4 shows a TEM view of such a macrocrack after annealing. Weldon *et al.* further propose that blistering is the effect of pressure building up in such cracks. By using in situ mass spectrometry during the annealing they observed a massive burst of molecular hydrogen coincident with the appearance of exfoliation. The liberated amount of molecular hydrogen was found to be only 30% of the initial hydrogen.

Zheng *et al.* [69] investigated the possible influence of wafer orientation on the characteristics of hydrogen implanted silicon. Silicon wafers with orientations of (100), (110) and (111) were implanted with hydrogen doses between $2 \times 10^{16} \text{cm}^{-2}$ and $8 \times 10^{16} \text{cm}^{-2}$ at either 40 or 50keV. Blister formation upon annealing, stress due to implantation, defects and damage due to implantation and layer transfer were investigated by using optical, electron, atomic force microscopy, ion scattering and infrared spectroscopy. Samples were implanted at 50keV to a dose of $6 \times 10^{16} \text{cm}^{-2}$ and annealed at $350\text{-}600^\circ\text{C}$ to measure the time

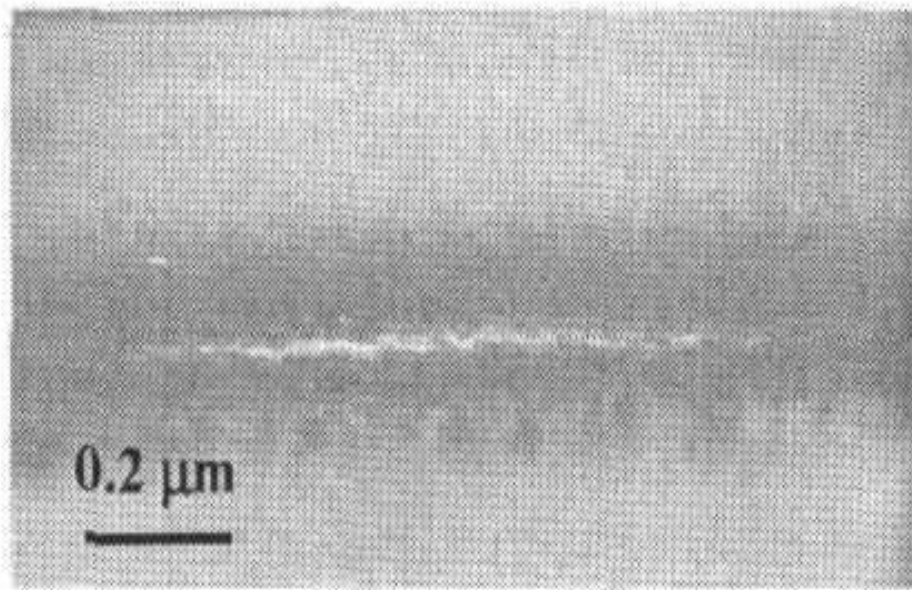


Figure 4.4: *TEM view of a macrocrack after annealing (from [9])*

necessary to produce blistering. The time for the (100) orientation was found to be the shortest, followed by the (111) and the (110) oriented wafers. TEM investigation of samples implanted with $6 \times 10^{16} \text{cm}^{-2}$ at 40keV shows platelets lying in the (100) and (111) direction in the case of the (100) oriented wafer and little or no evidence for platelets was found in the case of the (111) and (110) oriented wafer (Fig.4.5), which is consistent with the measured times. Infrared spectroscopy (IR) leads to three similar spectra which indicates that wafer orientation has no effect on the Si-H complex formation in the as-implanted wafer.

In contrast to IR spectroscopy, which is not sensitive to the presence of molecular hydrogen, forward recoil scattering (FRS) shows the total amount of hydrogen. Fig.4.6 shows the total amount of hydrogen and the IR active amount as a function of the annealing temperature. The amount of bound hydrogen decreases monotonically above 200°C, while the total amount stays constant up to 400°C. Weldon *et al.* [11] interpret this as a net conversion of Si-H into H₂ between 200°C and 400°C which remains trapped in the lattice. Since there is only a very small solubility of H₂ in silicon at room temperature Weldon *et al.* propose that the hydrogen must be bound in internal voids or cavities.

The exact cut-location after splitting of a bonded wafer has been extensively studied by Höchbauer *et al.* [71–74]. Samples were implanted at 175keV to a dose of $5 \times 10^{16} \text{cm}^{-2}$, bonded to a second wafer and then annealed at 600°C for 5min to achieve exfoliation. RBS was used to analyze the radiation-induced damage accumulation. Further, XTEM was used to obtain detailed information about the defects. Comparing results from Rutherford backscattering spectrometry (RBS) and XTEM Höchbauer *et al.* conclude that the cut location is near the center of the damage peak and not at the hydrogen concentration peak. Fig.4.7 shows a TEM image of the implanted region before and after splitting. It can be seen that the region which contains most of the defects belongs to the donor wafer after cutting. Only a small part of the defects is located in the exfoliated layer.

For the same experimental, elastic recoil detection (ERD) was performed to measure the hydrogen depth distribution. Compared to the damage profile the hydrogen peak about 5% deeper and very broad. This analysis also leads to conclusion that the cut location is near the center of the damage peak.

Further studies were carried out using samples implanted at 40keV to doses of $5 \times 10^{16} \text{cm}^{-2}$, $7 \times 10^{16} \text{cm}^{-2}$ and $1 \times 10^{17} \text{cm}^{-2}$ and annealed for 30min at 600°C to produce blisters. RBS, ERD and secondary electron detection (SED) were used to investigate the depth of "popped-off" blisters. Comparison of damage and hydrogen concentration with the cut location shows, that cutting takes place at the damage peak or at the deeper part of the hydrogen concentration, but never at the hydrogen peak (see Fig4.8). Interestingly Höchbauer *et al.* reported that for the middle dose two cut locations are visible, which means, that there is no smooth cut in this case.

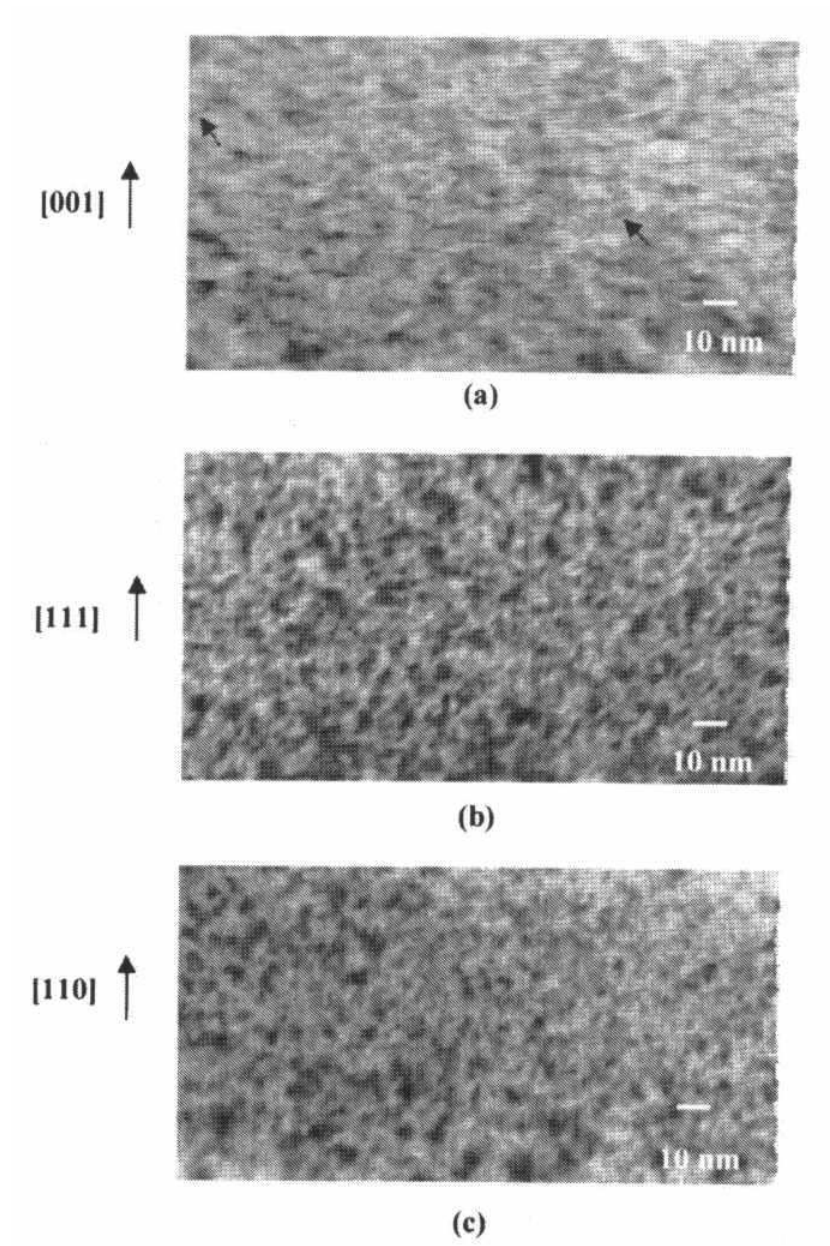


Figure 4.5: TEM view of platelet distributions for different wafer orientations after hydrogen implantation (from [69])

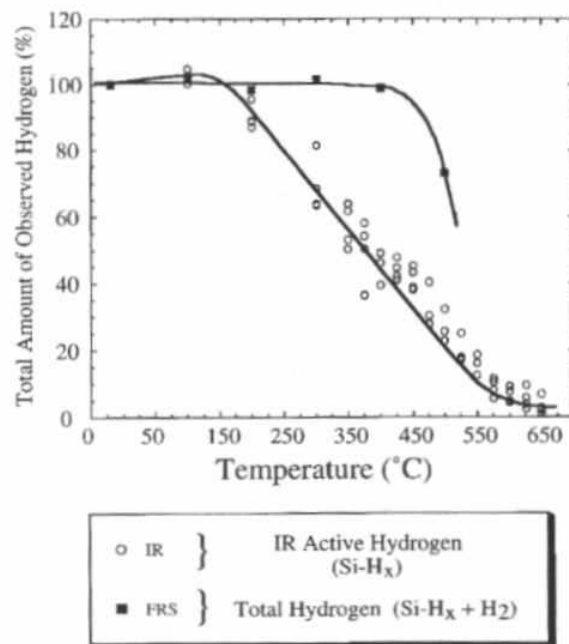


Figure 4.6: Transformation of hydrogen during annealing (from [11])

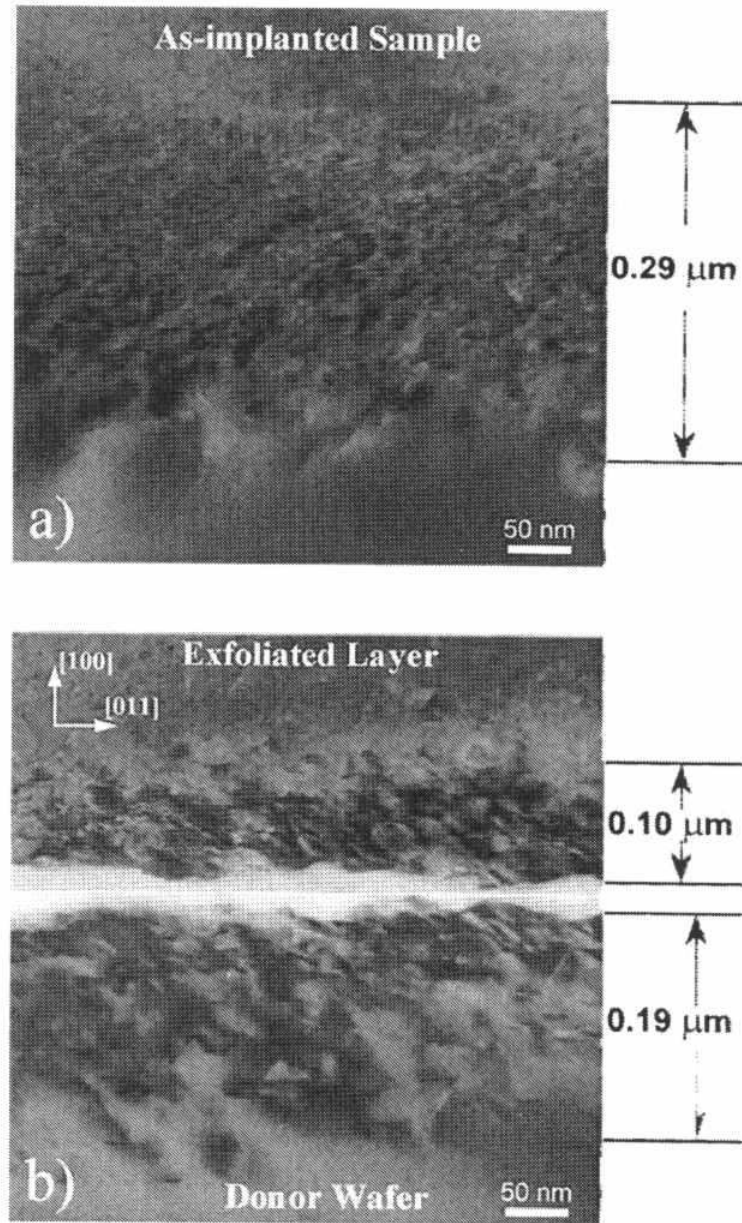


Figure 4.7: Location of the H-induced splitting (from [72])

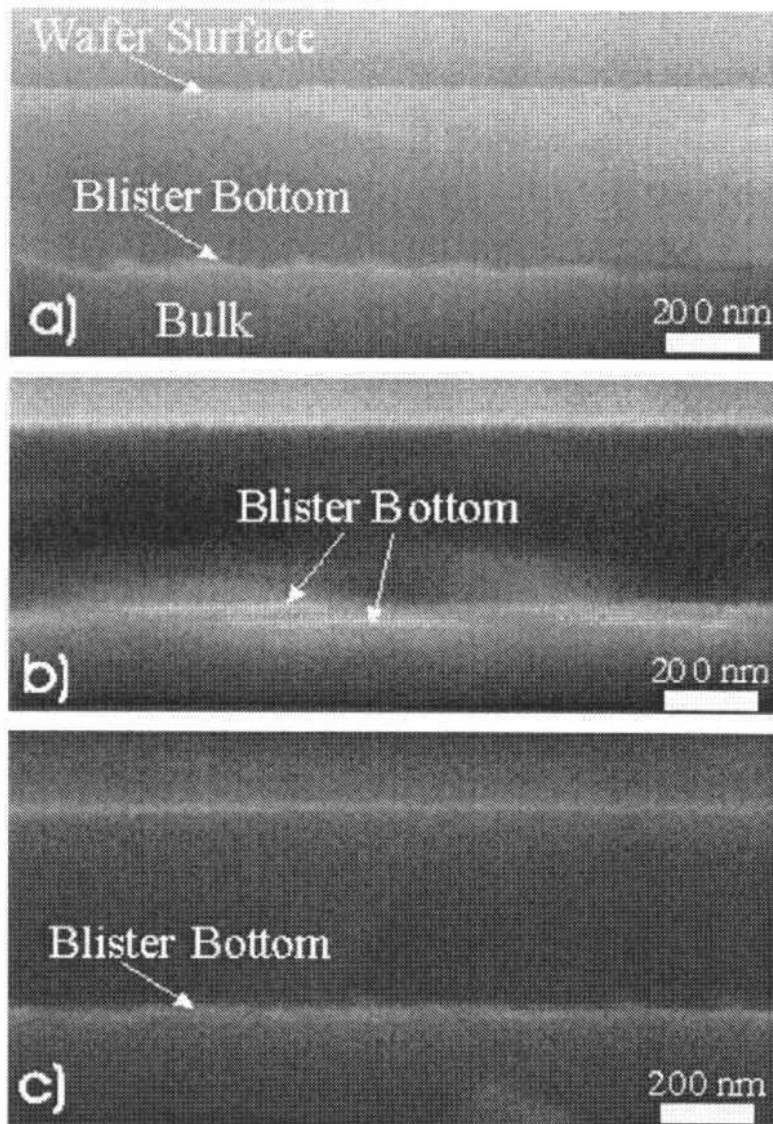


Figure 4.8: TEM view of “popped” blisters (from [74])

A more detailed study of the annealing behavior of hydrogen platelets using IR spectroscopy was done by *Weldon et al.* [11]. While the assignments of spectral lines is still discussed, there is a consensus that discrete modes are associated with isolated point defects of the form V_xH_y or IH_y , whereas the broad absorption is due to hydrogen trapped in a highly defective Si region. Point defect mode intensity is largely invariant with dose, whereas the multivacancy signature scales with the hydrogen concentration.

Fig.4.9 shows the IR spectrum of a sample implanted with a low dose of $2 \times 10^{16} \text{cm}^{-2}$ and Fig.4.10 of a sample implanted with an intermediate dose of $6 \times 10^{16} \text{cm}^{-2}$ as a function of annealing temperature. The assignment of the modes before annealing is shown in Tab. 4.1. The feature at 2106cm^{-1} occurs in a frequency range usually ascribed to hydrogen bound to internal silicon surfaces. Therefore *Weldon et al.* assign this feature to hydrogen terminating 50-100Å platelets as seen in the TEM image (Fig.4.2). After annealing up to 300°C attenuation of the broadband, multivacancy structure and a complete loss of the H_2^* modes can be observed. The VH_3/VH_4 modes are enhanced relative to the as-implanted spectrum. This indicates that there is a loss of bound hydrogen and an agglomeration of the remaining bound hydrogen at remaining vacancies. This trend continues at annealing up to 425°C where the complete attenuation of the broadband region takes place. The spectrum is then dominated by the VH_3/VH_4 modes.

Further annealing reveals a difference between the high and the low dose implantation. In the case of the low dose the VH_3/VH_4 modes disappear without the formation of new modes. In the case of the high dose the loss of the VH_3/VH_4 modes is accompanied by the formation of new modes at 2109cm^{-1} and 2119cm^{-1} . These modes collapse leaving a mode at 2104cm^{-1} with a shoulder at 2091cm^{-1} and a broader band at 2074cm^{-1} .

The mode at 2104cm^{-1} is replaced by a sharper peak at 2098cm^{-1} and a new mode at 2083cm^{-1} at annealing upon 650°C . These assignments indicate, that the dihydride Si(100) surfaces undergo a 2×1 reconstruction to form hydrogen terminated Si(100) surfaces. These modes observable for the high dose upon annealing are absent in the case of the low dose but appear for doses between $1 \times 10^{17} \text{cm}^{-1}$ and $1.8 \times 10^{17} \text{cm}^{-1}$ at lower temperature, for which blistering takes place at 400°C and 450°C .

Based on their experiments *Weldon et al.* [11] propose the following mechanism of nucleation and growth of platelets:

Implantation of hydrogen predominantly produces multivacancy structures. Upon annealing between 200 and 350°C this region liberates molecular hydrogen and small cavities evolve where the molecular hydrogen is trapped. Internal (100) and (111) surfaces are formed out of agglomerated monovacancy defects which partly evolved out of the initial multivacancy defect structure. The molecular hydrogen agglomerates in these defects resulting in sufficient pressure for

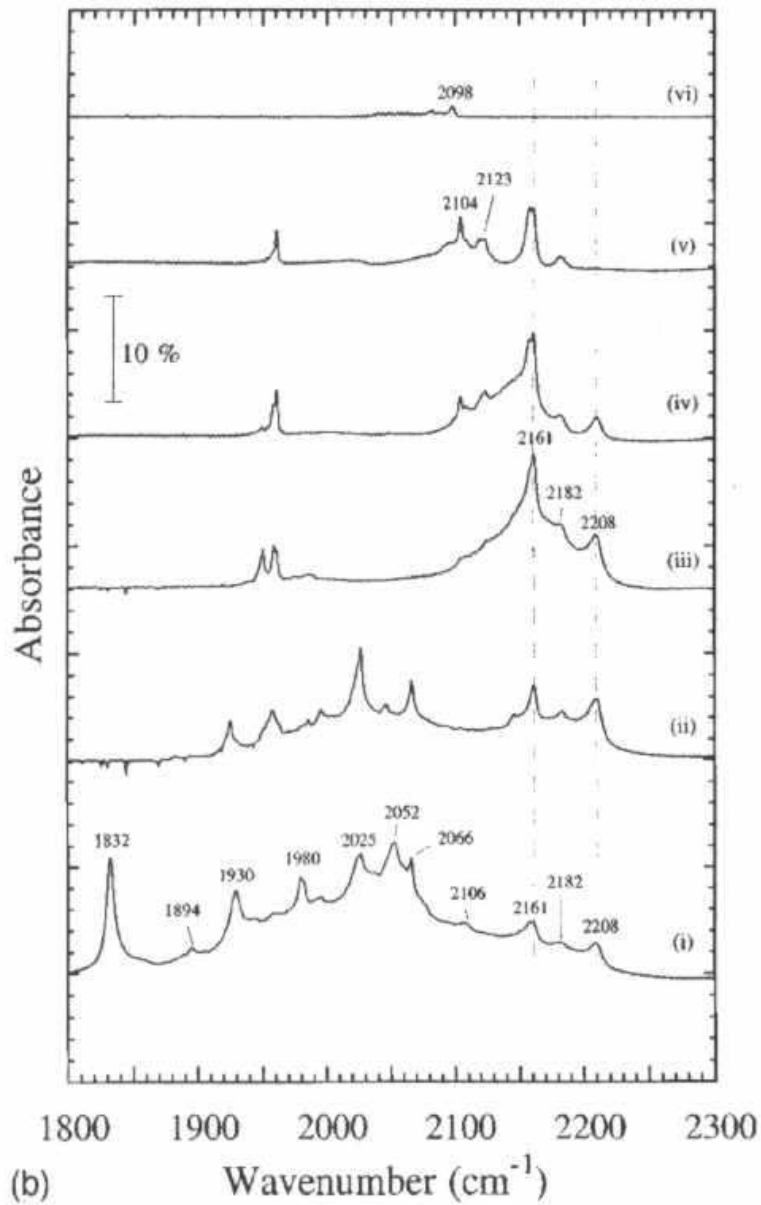


Figure 4.9: IR spectra of the Si-H stretching modes of hydrogen implanted Si at a dose of $2 \times 10^{16} \text{ cm}^{-2}$ at (i) room temperature and after annealing to (ii) 300°C (iii) 425°C (iv) 500°C (v) 550°C (vi) 650°C (from [11])

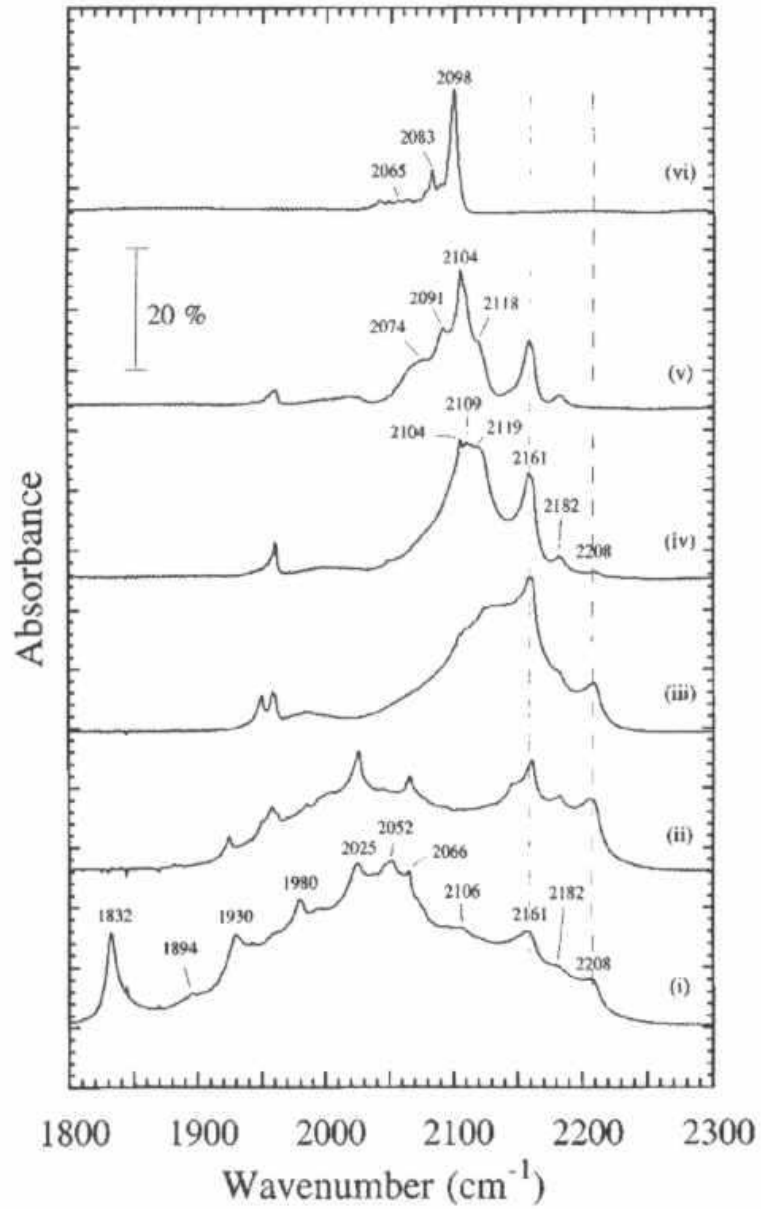


Figure 4.10: IR spectra of the Si-H stretching modes of hydrogen implanted Si at a dose of $6 \times 10^{16} \text{ cm}^{-2}$ at (i) room temperature and after annealing to (ii) 300°C (iii) 425°C (iv) 500°C (v) 550°C (vi) 650°C (from [11])

mode	defect
1832/2052cm ⁻¹	H ₂ *
2066cm ⁻¹	VH
2161/2182cm ⁻¹	VH ₃
2208cm ⁻¹	VH ₄
2106cm ⁻¹	hydrogenated internal surfaces
1930/2025cm ⁻¹	V ₂ H, V ₂ H ₂

Table 4.1: Spectral features before annealing (from [11])

modes	defect
2074/2098cm ⁻¹	coupled monohydride species on the atomically smooth terraces and along the steps of a Si(100) surface
2091/2104cm ⁻¹	dihydride terminated Si(100) surface
2109/2119cm ⁻¹	symmetric and asymmetric Si-H ₂ stretching motions, atomically rough (100) surfaces
2083cm ⁻¹	atomically flat Si(111) surfaces

Table 4.2: Spectral features upon annealing up to 650°C (from [11])

blistering.

Similar observations can be made for annealing samples implanted with low energy (see Chapter 3). Moutanabbir *et al.* [5–7] observed attenuation of the low-frequency band, assigned to hydrogenated multivacancies upon annealing to 300°C in the case of hydrogen implantation. Annealing to 400°C shows further attenuation of these defects accompanied by a rise of peaks assigned to hydrogenated monovacancies, especially VH₄ defects. Upon further annealing features assigned to VH₃ or V₂H₆ become dominant, together with features at ~2120cm⁻¹, which is according to Weldon *et al.* an important feature in the blistering/splitting process. From these assignments Moutanabbir *et al.* conclude that VH_n defects are involved in the nucleation of platelets.

In the case of deuterium implantation an attenuation of the low-frequency broadband upon annealing up to 300°C can be observed as well. However, the intensities of the features assigned to VD₃ or V₂D₆ and VD₄ remain too weak to trigger blistering. In contrary to hydrogen, some deuterium is still present at high temperatures bound in ID₂. For the implantation of a high dose of deuterium a similar behavior can be observed, but at annealing at 470°C a discrete spectral feature at 1544cm⁻¹ appears, which is assigned to a coupled monodeuteride mode of deuterium trapped on extended internal surfaces. Moutanabbir *et al.* conclude, that the deuterium which is released during annealing is re-trapped on extended internal surfaces.

In summary the following important information concerning the nucleation and growth of hydrogen platelets have been deduced from experiments.

- Implanting hydrogen into silicon produces extended defects unrelated to either plasma or radiation damage
- Defects lie in the (100) or (111) planes, centered around the mean projected range of hydrogen ions R_p
- Defects appear to be microcracks and are referred to as hydrogen platelets
- (100) platelets grow during annealing forming a macrocrack
- (111) platelets do not grow
- Spectroscopy shows that platelets consist of Si-H bonds
- Evolution of absorption modes could reveal the nature of platelet evolution but assignment of spectral features to defect structures is still under discussion
- At annealing between 200°C and 400°C a transformation of bound hydrogen into molecular hydrogen takes place
- H₂ agglomerates inside the macrocracks and builds up pressure resulting in blistering/exfoliation
- In the case of splitting the cut takes place near the maximum of the implantation damage

4.3.2 Blistering and splitting kinetics

The annealing time necessary to achieve splitting was studied by Aspar *et al.* [70]. Parameters as implantation dose and energy, doping level and bonding parameters were taken into consideration. A wafer was implanted under standard conditions and then bonded to a second wafer. During annealing two different activation energies were obtained from an Arrhenius-type plot (see Fig4.11), which indicates that there are two different mechanisms involved. At temperatures below 500°C the activation energy is about 2.5eV, at high temperature 0.5eV. Variations of the implantation energy does not alter the activation energies. Variation of other parameters like dose leads to a different activation energy at low temperature, while the activation energy for high temperatures always stays the same. Aspar *et al.* conclude that the activation energy of 0.5eV, which is comparable to the migration energy of hydrogen at high temperatures ($\sim 0.48\text{eV}$) indicates control of splitting by atomic hydrogen diffusion at high temperatures. At low temperatures different activation energies are obtained, dependent on process parameters. This mechanism also involves hydrogen diffusion, but this diffusion is trap-limited.

Freund [63] derived an equation for a lower bound of the density of implanted hydrogen atoms to induce wafer splitting. The magnitude of gas pressure in the platelets necessary for driving the fracture over the whole wafer is calculated.

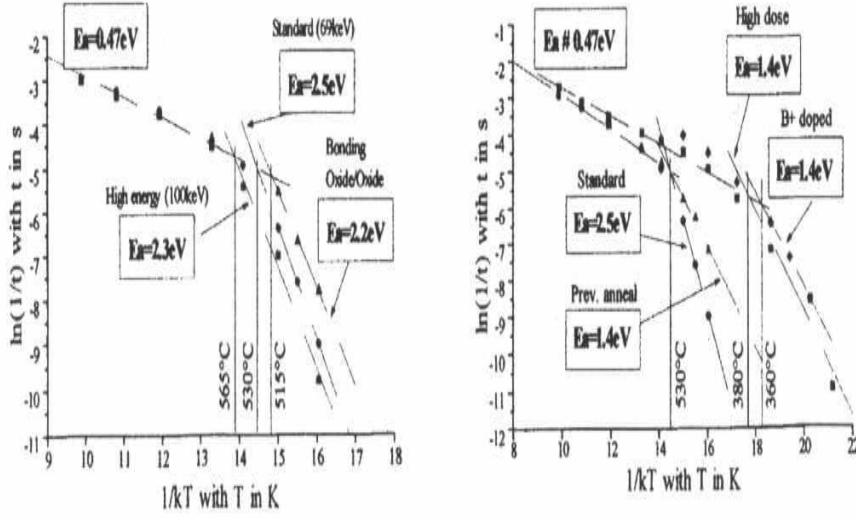


Figure 4.11: Activation energy for layer splitting (from [70])

Freund focused on the question of the minimum dose required for fracture if all hydrogen is available for inducing pressure in the platelets. A platelet is therefore considered as a crack in a nominally elastic material with shear modulus μ and Poisson ratio ν . In the case of pressure absence the crack is closed and the material is unstressed (see Fig.4.12). Considering the implantation of J atoms per unit area there is some minimum value for J

$$J_{min} = \frac{8}{3} \frac{\gamma}{kT} \quad (4.7)$$

such that the growth of a crack is limited if $J < J_{min}$, whereas a crack can grow across the whole wafer if $J > J_{min}$. In Eq.4.7 γ is the surface energy density, k the Boltzmann's constant and T the absolute temperature.

Yang [65] focused on the effect of external stress on the wafer splitting and the effect of molecular hydrogen formation on the nucleation of microcracks by using the linear elastic theory and thermodynamics. The model is similar to that used by Freund (Fig.4.12). Resulting from various calculations it can be seen that the critical nucleation size of a microcrack increases with the adhesion energy and the elastic modulus of the material, while tensile stress and internal pressure due to molecular hydrogen decreases the critical size. Further, the critical nucleation size increases with temperature and is inversely proportional

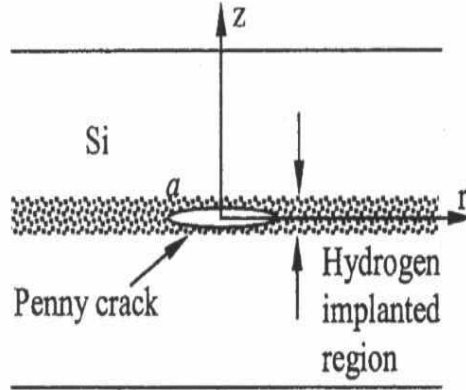


Figure 4.12: Simple platelet model (from [63])

to the fourth power of the dose of implanted hydrogen. Considering the growth of a microcrack, the critical amount of necessary hydrogen is proportional to the square of the crack size and inversely proportional to temperature.

Varma [64] derived the conditions of anisotropic growth of H_2 bubbles leading to exfoliation or blistering based on a platelet model shown in Fig.4.13. Surfaces with Si-H bonds are weakly bonded to similar surfaces with substantial anisotropic voids in which H_2 agglomerates. A single bubble with N hydrogen molecules at a temperature T is described through its surface energy γ and the elastic parameters of bulk-Si. Out of this model equations for blistering and splitting were derived.

Tong *et al.* [66] investigated the annealing time required to produce hydrogen-induced optical surface blisters in unbonded samples and exfoliation in bonded samples. For various temperatures the effective activation energy E_a was determined through the relation

$$1/t_b \propto \exp(-E_a/kT) \quad (4.8)$$

where t_b is the time required to show blisters/splitting (also denoted as onset-time), k the Boltzmann constant and T the absolute temperature. The activation energy for both processes is the same and is close to the bond energy of silicon. The time required for layer splitting is about ten times longer than the time required to show optically detectable blisters (Fig. 4.14).

From the investigations of the blistering time the question arises, whether microcracks pop up as surface blisters after the onset-time or the onset-time is just a parameter associated with optical resolution. To answer this question Huang *et al.* [67] used a combination of optical microscopy and atomic force microscopy (AFM). Optical microscopy shows that blisters do not form until the onset-time is reached. Upon this point blisters suddenly appear, grow with

further annealing and finally break. To ensure that this is not connected to optical resolution limitation the surface morphology was studied with AFM. This investigation clearly showed that the occurrence of blisters is a sudden pop-up step at a critical time and not a gradual growth process (Fig.4.15). Based on published TEM results and their AFM data Huang *et al.* conclude that platelets grow in a closed form up to a critical size where the pressure is high enough to overcome the surface energy. The critical radius of a platelet can be calculated through an equation derived by Mitani and Gösele [68]

$$r_{crit} = \{16\gamma_p E t^3 / [9\alpha(1 - \nu^2)\Delta p^2]\}^{1/4} \quad (4.9)$$

where Δp is the difference between the pressure in the platelet and outside, γ_p is the surface energy associated with the interaction between hydrogen-covered surfaces, t corresponds to the hydrogen implantation depth, E is Young's modulus, ν the Poisson ratio and α a numerical factor. Eq.4.9 predicts that increasing the implantation depth also increases the critical size of the platelet which corresponds to the size of the first emerged surface blister. Fig.4.16 shows the comparison between critical sizes obtained by experiment and calculations as a function of implantation depth.

To sum up, the following conclusions arise from the theoretical investigations:

- Splitting is controlled by hydrogen diffusion
- A lower bound of the implanted dose required for forming a macrocrack can be calculated
- Occurrence of surface blisters is a sudden pop-up process
- The size of blisters increases with implantation depth

4.3.3 Platelet theories

H_2^* platelets

Zhang and Jackson [75] studied the nucleation and growth of hydrogen clusters by using pseudopotential total-energy calculations to find possible structures for (111) platelets. Fig.4.17 shows the possible candidates for platelets. Hydrogenated point defects were also considered, but due to high formation energy or high energy relative the other structures not further investigated. The formation energies of the double-layer H_2^* structure (Fig.4.17c) and the half-stacking fault (Fig.4.17d) are reported to be significantly lower than the formation energy of an interstitial H_2 molecule at the T_d site. Moreover the energy can be further reduced by lattice expansion. Although the half-stacking fault is the lowest energy configuration there seems to be no low-energy path to build this

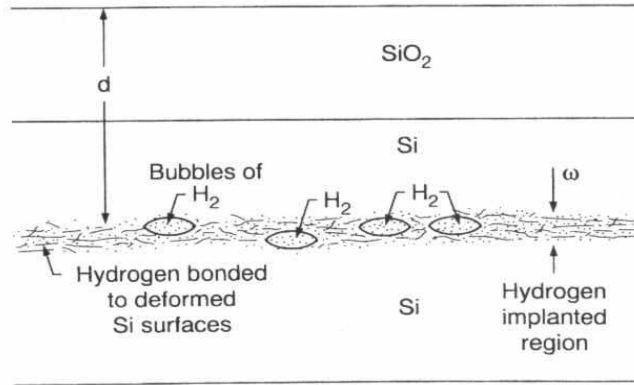


Figure 4.13: Model for hydrogen platelets (from [64])

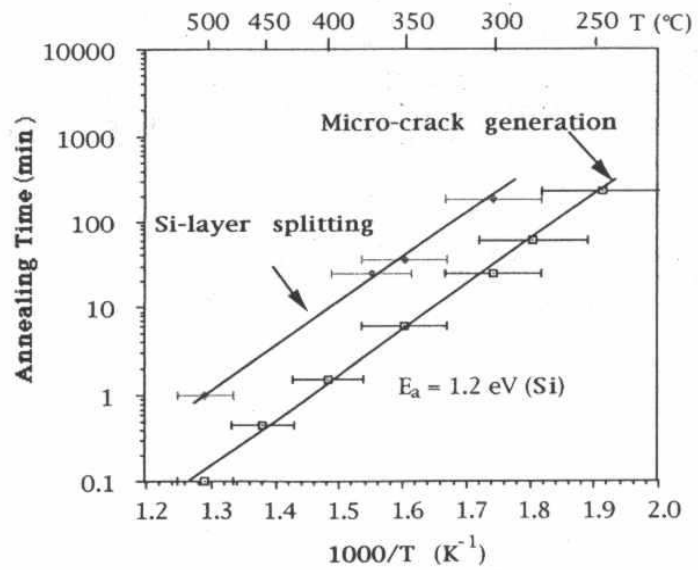


Figure 4.14: Activation energies for blistering/splitting (from [66])

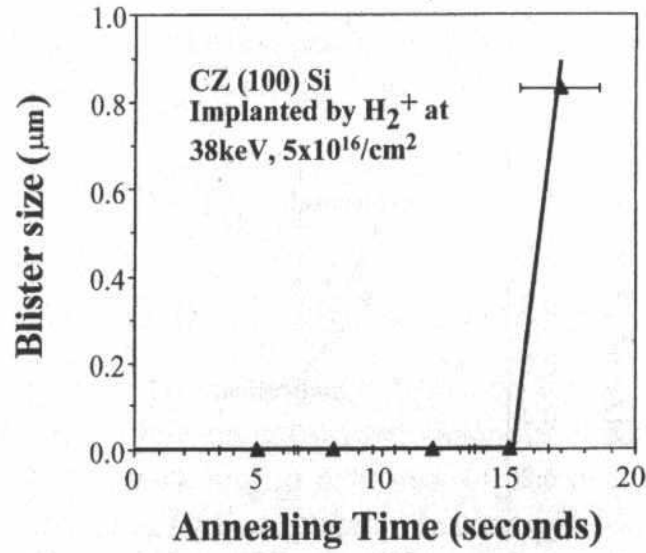


Figure 4.15: Onset-time for blistering (from [67])

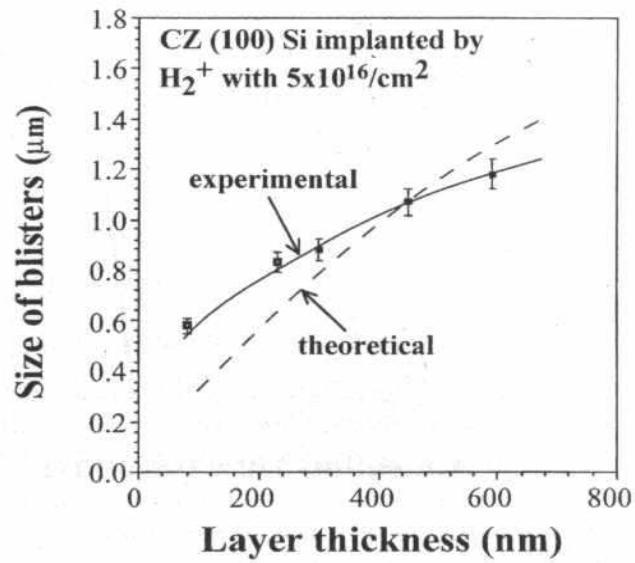


Figure 4.16: Critical size vs. implant depth (from [67])

structure without the preexistence of dislocations or line defects.

First-principle calculations on the transformation of $(\text{H}_2^*)^D$ into H-saturated internal surfaces were done by Kim and Chang [76]. The formation energy of possible platelet structures (see Fig.4.18) was calculated as a function of dilation. The $(\text{H}_2^*)^D$ structure becomes more stable as the number of H_2^* aggregates is increased. Kim and Chang considered this structure to be favored at the initial stage of platelet formation. As the dilation reaches a certain point, the $[\text{Si-H}]_n$ structure with H_2 between the planes ($[2\text{Si-H}+\text{H}_2]_n$ in Fig.4.18) is more stable, which indicates a structural transformation as the lattice is expanded. The lateral growth of the $(\text{H}_2^*)^D$ aggregate increases the lattice dilation, which makes at some point the $[\text{Si-H}]_n$ energetically favorable. This structure shows the important features observed in experiments for (111) platelets.

The so far unsolved problem of initial hydrogen condensation was investigated by Martsinovich *et al.* [78]. They considered finite H-aggregates, which are H_2^* aggregates in the glide plane and Si-H bonds in the shuffle plane. The structures are similar to Fig.4.19 but finite in the $[1\bar{1}0]$ direction. The lowest energy configuration among these structures is a pair of H_2^* defects, which spontaneously transforms into a 90° dislocation loop in the glide plane. Next, these structures were considered to be infinite in the $[1\bar{1}0]$ direction. The lowest energy configuration among these defects is the hydrogenated dislocation dipole. By using elastic theory Martsinovich *et al.* predict, that the hydrogenated dislocation loop can grow along the direction of the dislocation with a formation energy per hydrogen atom that converges towards the infinite limit of the formation energy of a hydrogenated dislocation dipole.

Further calculations [77] lead Martsinovich *et al.* to the conclusion, that the hydrogenated dislocation dipole can grow by glide, with hydrogen aggregating in the shuffle plane between the two dislocations forming Si-H bonds. This configuration is similar to the half-stacking fault proposed by Zhang and Jackson (Fig.4.17d).

Out of these considerations the following mechanism of (111) platelet nucleation and growth emerges:

- The lowest energy configuration of four hydrogen atoms are two H_2^* defects
- This pair of H_2^* defects transforms spontaneously into a 90° hydrogenated dislocation loop
- The hydrogenated dislocation loop prefers to grow in the direction of the dislocation forming a hydrogenated dislocation dipole
- The hydrogenated dislocation dipole expands through glide and transforms into a half-stacking fault

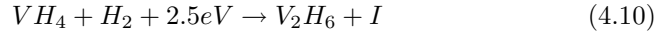
Although this half-stacking fault is the lowest energy configuration for a mid-size structure, the calculations of further growth were done based on the double-layer structure. This structure transforms into the $[\text{Si-H}]_n$ structure with H_2 between the planes, which shows the important feature of (111) hydrogen platelets. It is therefore not clear, whether there is such a transformation of the half-stacking fault as well, leaving a gap between the mid-size and larger platelet structures.

VH₄ platelet theory

Early theoretical investigations of the nature of (111) platelets have been done by Van de Walle *et al.* [32, 33]. Total energy calculations in a superlattice geometry have been performed for various possible platelet structures. They suggest that the vacancy-formation mechanism is likely to be involved in the platelet formation, but could not make any further conclusions.

Based on the experimental results discussed in Section 4.3 and first-principle calculations Reberedo *et al.* propose a theory of platelet nucleation involving VH₄ defects [79].

A single VH₄ can be involved in several processes. The lowest energy reaction for arrival of the first H₂ molecule is:



For the next arriving H₂ a similar reaction can take place:



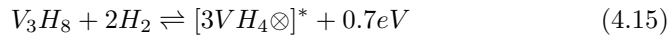
This reaction can be repeated for each H₂ molecule, leading to the formation of an H void. Every step involves the emission of an interstitial. An alternative reaction without emitting an interstitial and lower energy is:



The reaction is possible in both directions with the same activation energy. VH₄ \otimes VH₄ denotes two second-neighbor VH₄ defects. Since the formation energy of this complex is twice the formation energy of a VH₄ defect, two VH₄ defects will not bind to each other. The complex can only be formed via the V₂H₆ defect. Therefore Reberedo *et al.* deduce that the repetition of Eq.4.10 and Eq.4.12 will lead to the formation of an aggregate of second-neighbor VH₄ defects. In the diamond lattice structure three second-neighbor VH₄ defects define either a (100) or (111) plane.



It is also possible that VH₄ aggregates evolve out of the mini H void V₃H₈ through



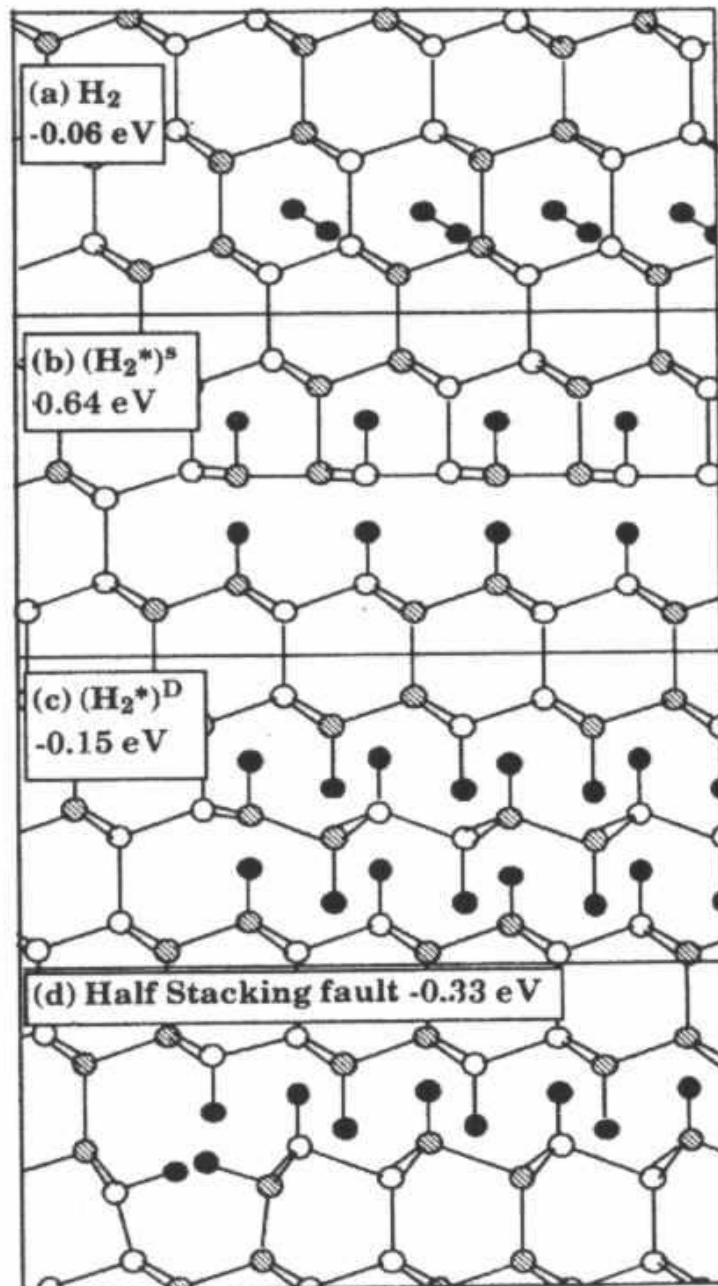


Figure 4.17: Possible structures for (111) hydrogen platelets (from [58])

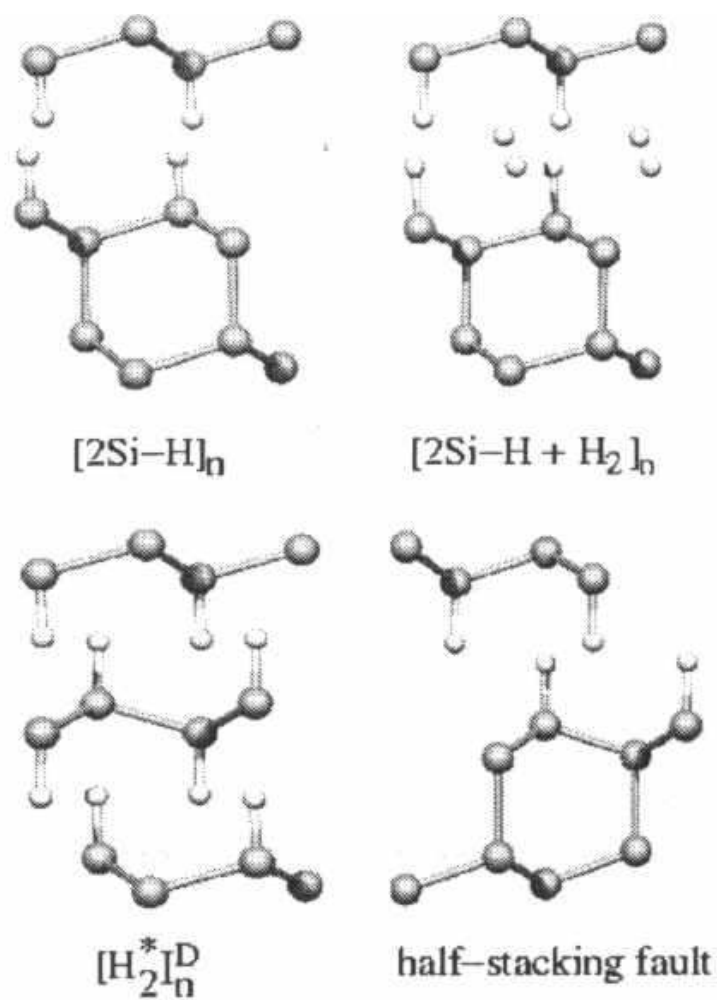


Figure 4.18: Structures for mid-size and larger platelets (from [77])

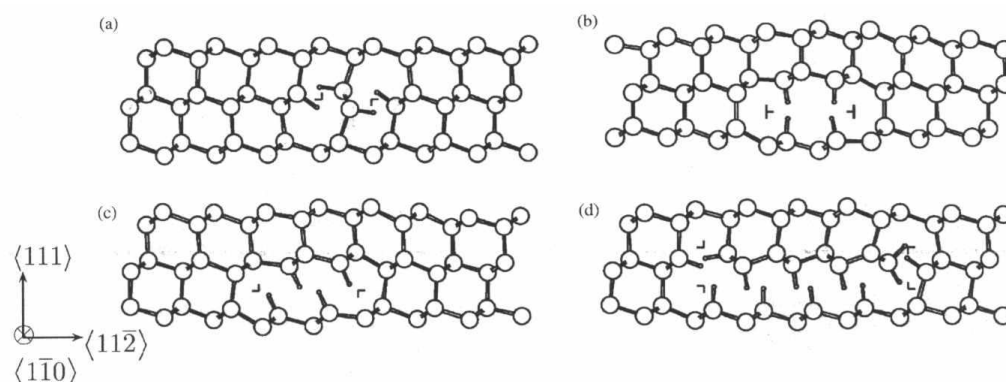


Figure 4.19: Structures for finite number of hydrogen atoms (from [78])

where $[3\text{VH}_4\otimes]^*$ stands for three second-neighbor VH_4 defects forming a primitive face of a tetrahedron, which could be an alternative seed for a (111) platelet. To identify the mechanisms of further growth in larger platelets the formation energy per VH_4 was calculated as a function of the separation of the two opposing surfaces. The result shows that relaxation leads to an energy gain for the (100) and the (111) direction. No energy gain is possible for a random structure of the agglomerated VH_4 defects. Reberedo *et al.* conclude that this fact makes a planar array of second-neighbor VH_4 energetically preferable.

The accumulation of H_2 as observed by Weldon *et al.* is naturally accounted for in terms of vacancy platelets. It is well known that hydrogenated (100) surfaces undergo a 2×1 reconstruction, during which half of the amount of hydrogen is released. Reberedo *et al.* expect opposing faces of large vacancy platelets to undergo such a transformation and conclude that the proposed structures exhibit all features of the observed hydrogen platelets.

4.3.4 Discussion of the isotope effect

As seen in Chapter 3 hydrogen agglomerates in multihydride monovacancy structures, which are precursors of hydrogenated extended internal surfaces. Deuterium binds preferably to multivacancy structures, resulting in highly stable structures, which are useless for blistering.

A possible explanation for the isotope effect is the different amount of the implantation damage. Since the average distance between vacancies produced by deuterium implantation is 30% shorter than for hydrogen, the probability of the formation of divacancies is much higher. Moutanabbir *et al.* point out that it is well known that a single vacancy is mobile at room temperature, whereas the divacancy is not. This could be a reason for the preferred binding of deuterium to multivacancies.

Another possible effect is based on the VH_4 platelet theory. These structures consisting of m second-neighbor VH_4 defects become more stable as they grow, but the reaction is also reversible. Therefore the process must take place rapidly, requiring an order of reaction m . A small isotope effect could be amplified to the power m .

Chapter 5

Simulation

As will be shown in the next section, simulation is an important tool for gaining information about the physical mechanisms underlying blistering/splitting. Furthermore, once calibrated and tested, simulation can be used to optimize process parameters and to investigate effects of process variations. In this section the desirable features of a simulation tool are discussed, the simulation tools and methods are introduced and the setup of the simulation done in this thesis is presented.

5.1 Goals for the simulation of hydrogen platelet nucleation and growth

For the purpose of simulating platelet nucleation and growth the desirable features would be e.g.:

- Illustration of initial platelet distributions after implantation at room temperature, comparable to TEM pictures obtained by experiments
- Visualization of platelet size and distributions for various time steps during simulation of annealing
- Calculation of the surface modification in the case of unbonded wafer and simulation of the splitting in the case of a bonded wafer

However, since the physical nature of hydrogen platelets is still unclear, these features of a simulation tool can only be future goals. At the moment more immediate goals are the simulation of the distribution of defects after implantation and the evolution of these defects during the annealing process. The simulation results can be compared to defect distributions obtained by spectroscopical analysis and may give insight into the mechanisms of defect formation and transformation.

Such a simulation could for instance be done in regard to the thermal evolution of the IR spectra and the corresponding defect assignments proposed by Weldon *et al.* (Fig.4.9 and Fig.4.10), where the following goals for the simulation could be set up according to experimental data.

- Attenuation of the multivacancy defect structure, enhancement of VH_3/VH_4 and complete loss of H_2^* up to $300^\circ C$
- Complete attenuation of the multivacancy defect structure, dominance of VH_3/VH_4 defects up to $425^\circ C$
- Rearrangement of the defect structure into internal hydrogenated Si(100) surfaces up to $500^\circ C$
- Reconstruction of the Si(100) surfaces into atomically flat Si(111) surfaces up to $600^\circ C$

In addition, the isotope effect discussed in Chapter 3 provides data well suited for simulation. Since implantation of hydrogen and deuterium to the same dose leads to blistering in the first case and to no visible surface alteration in the second, an important mechanism for the nucleation and growth of the hydrogen platelets could be obtained by comparing the results of the simulation of these two implantations.

Since there are too many uncertain parameters that are essential for the simulation of the annealing steps this work concentrates hydrogen/deuterium implantation at room temperature. From these considerations the following simulation goals emerged:

- Calculate defect distributions and compare with the experimental results
- Confirm or disprove the theory about the isotope effect of hydrogen induced blistering, which also includes the theory about VH_4 defects
- Confirm or disprove the theory about H_2^* platelets

5.2 Simulation methods and tools

The implantation of ions produces fast developing collision cascade, which have to be modeled accurately. These cascades and the resting positions of the ions, vacancies and interstitials are simulated by using the binary collision approximation (BCA). Further, these defects diffuse, which has to be simulated as well. Since the implantation and annealing of a wafer takes several minutes and only small defects are produced during the impacts, molecular dynamics simulations (MD) are not feasible. This thermal activity can be better simulated by using kinetic Monte Carlo simulation (kMC). In this thesis a coupling of binary collision simulation and kinetic Monte Carlo simulation is used.

5.2.1 IMSIL

The IMSIL (IMplant SIMuLator) program is based on the binary collision approximation. The simulation of atoms or molecules into targets composed of a crystalline region with a diamond lattice structure and an arbitrary number of amorphous regions is possible. The damage produced by ions can be taken into account dynamically for simulation of subsequent ion trajectories [80]. Details about the physical model implemented in IMSIL can be found in [81]

To describe the path of an ion through the crystal the binary collision approximation is used [82]. The collision is treated as a classical two-body problem with an interatomic potential which includes classical and quantum mechanical terms. Ions scatter from target atoms and are further slowed down by the interactions with electrons of the target atoms.

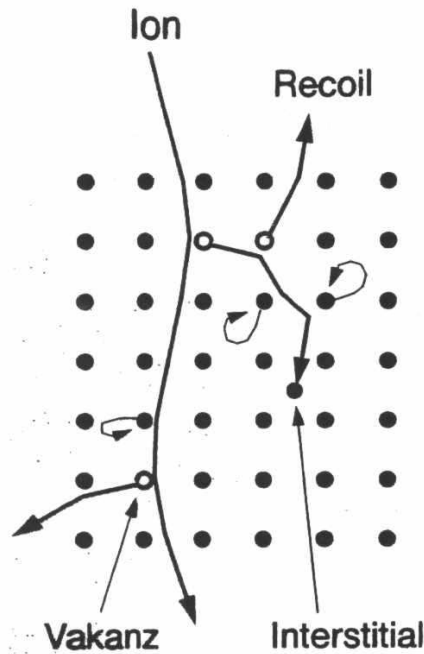


Figure 5.1: *Binary Collision (from [82])*

Fig. 5.1 shows the possible interactions of the ion with the target atoms. A target atom can either remain at its original site or recoil, if the energy transferred in the collision exceeds the displacement barrier ($E_d=15\text{eV}$). A recoil leaves behind a vacancy, and forms an interstitial when it stops.

The complete motion of the ion is calculated as a series of binary collisions until all the atoms come to rest. The true trajectory segments are approximated by

straight lines.

The statistical variation of the implantation is given by the random entry points of the ions and by the lattice vibrations. The position of a target atoms is calculated through

$$\vec{x}_A = \vec{x}_L + \begin{pmatrix} R_{g1} \\ R_{g2} \\ R_{g3} \end{pmatrix} * U_1 \quad (5.1)$$

where \vec{x}_L is the lattice site and R_{g1}, R_{g2}, R_{g3} are Gaussian distributed random numbers, and U_1 is the mean vibration amplitude in one direction, which can be calculated from Debye theory.

By combining the resting positions of the ions and interstitials a final distribution can be achieved, which can either be printed in a histogram or the atomic positions of the ions are stored in a file [80].

5.2.2 Kinetic lattice Monte Carlo simulator (kLMC)

This tool was written by Gustav Otto [83]. Necessary enhancements for the simulation of hydrogen implantation were made for the purpose of this thesis.

The principle of kinetic Monte Carlo simulation [85, 86] is illustrated in Fig.5.2 which shows in the upper part the TEM image of a $\{311\}$ defect in silicon. In contrast to MD simulation that treats all atoms, only isolated point defects and point defects belonging to extended structures are marked and transferred to the simulation. Monte Carlo simulation is an event driven simulation method, which means that events like diffusion hops are simulated. In the example shown in Fig.5.2 isolated point defects would jump to a neighbor position (e.g. with a mean period of 10^{-9} s at elevated temperatures). Point defects may be emitted from the extended defect at some longer mean period (e.g. 10^{-3} s). To accurately describe this defect behavior it is necessary to know the energy values for binding and diffusion, which are either obtained from calculations (*ab initio* or MD) or fit to experimental data. Fig.5.3 shows the energies involved in the basic reactions of a point defect with a foreign atom. In this example a migrating free interstitial captures a substitutional B atom and forms an IB complex that may be mobile or not.

The decision which event is next is made according to the event rates, which are calculated directly from the energies. For instance the jump rate of a point defect is calculated through

$$J_{rate} = \frac{6}{\lambda^2} * D_0 * e^{-\frac{E_{mig}}{kT}} \quad (5.2)$$

where D_0 is the diffusion prefactor, E_{mig} the migration energy and λ the jump distance.

The main advantage of the Monte Carlo approach is that real process time intervals can be simulated while atomic scale parameters from *ab initio* calculations can be used. In the kLMC simulator information about the lattice is also included. Therefore defects can only be located at lattice sites [83].

Fig.5.4 shows the basic simulation flow of the kLMC program.

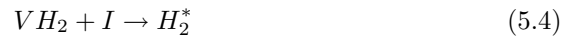
- DLS (Defect Lattice Site), like vacancies, interstitials or foreign atoms are read in
- DLS belong to the same defect if they are located at neighboring lattice sites, otherwise they are identified as point defects
- The event rates are calculated according to Eq.5.2
- For each defect and each event of this defect an event time is calculated through

$$time = -\frac{\ln(R_n)}{P} \quad (5.3)$$

where R_n is a random number between 0 and 1 and P is the event rate

- Next, the event which has the shortest event time is selected and executed
- Inside a certain radius all DLS and defects possibly affected by this event are marked and checked if new DLS and defects were created
- For these new DLS and defects the event rates are calculated
- For the defects inside this radius the event time is re-calculated using Eq.5.3
- For the defects outside, the event time is set to $t' = t - \Delta t$

The kLMC program analyzes the defect lattice sites, which include for example interstitials, vacancies or hydrogen atoms at a lattice site, and writes clusters of the form $V_i I_j H_k$ to the output file. With the restriction that vacancies and interstitials in the same cluster recombine, the output is either $V_i H_k$ or $I_j H_k$ with $i, j, k \geq 0$. Based on this output it is investigated whether there are isolated defects, which are counted and separately listed. In the kLMC program the H_2^* defect can evolve out of a VH_2 or an IH_2 defect through [50]:



Tab.5.1 shows the possible defect types that can form during the simulation of hydrogen implantation. Clusters can capture and, in principle emit point

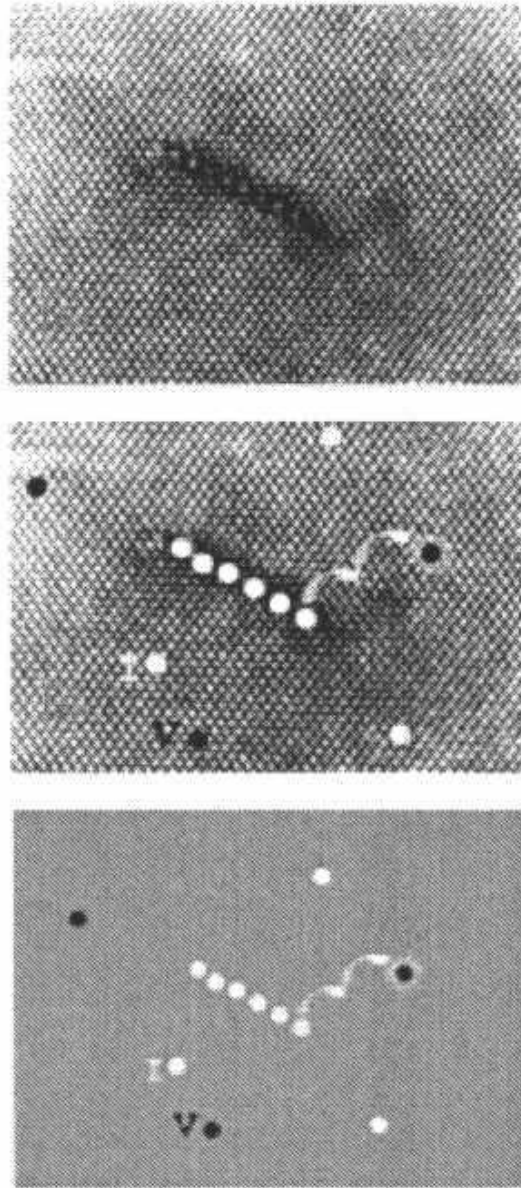


Figure 5.2: *kMC* concept:(a) shows a *TEM* view of a $\{311\}$ defect, circles in (b) and (c) represent the defect atoms simulated by Monte Carlo (from [86])

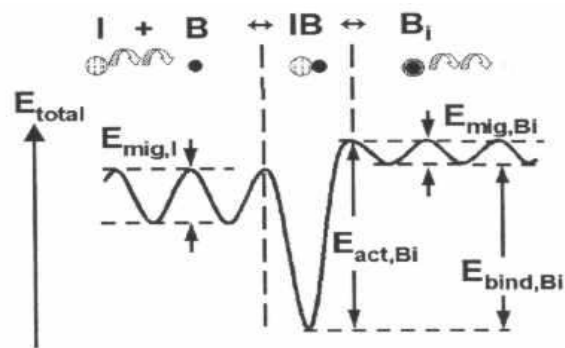


Figure 5.3: Energy parameters for kinetic Monte Carlo simulation (from [86])

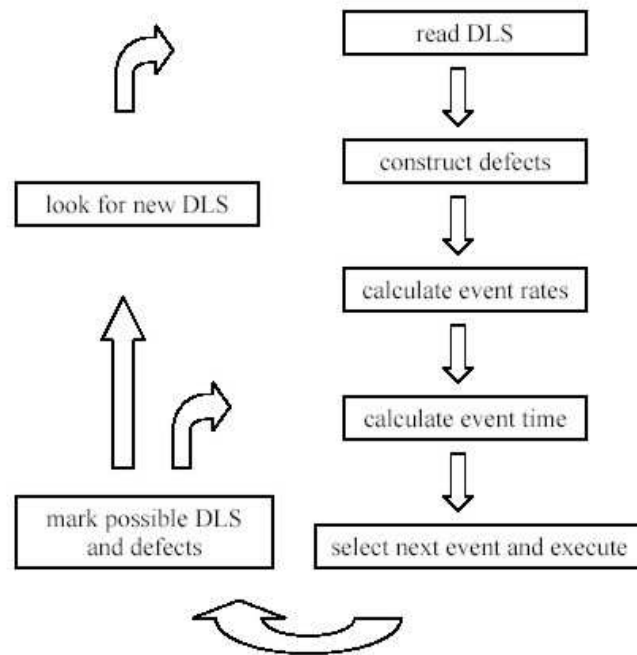


Figure 5.4: Simulation flow of kinetic Monte Carlo simulation

Interstitials	I
Vacancies	V
Atomic Hydrogen	H
	H_2^*
Molecular Hydrogen	H_2
Hydrogen saturated Vacancies	VH, VH ₂ , VH ₃ , VH ₄
Hydrogen saturated Interstitials	HI, H ₂ I, H ₃ I, H ₄ I
Hydrogen saturated Multi-Vacancies	$V_i H_k$
Hydrogen saturated Multi-Interstitials	$I_j H_k$
Vacancies clusters	V_i
Interstitial clusters	I_j

Table 5.1: Possible defects for the simulation of hydrogen implantation

defects. The emission, however, is unlikely at room temperature. Interstitials and vacancies can recombine if they are located within the same cluster or they can jump to neighboring lattice sites. For the simulation of implantation at room temperature the simplification can be made that defects do not dissociate.

5.3 Setup of the simulation and simulation parameters

As mentioned at the beginning of this section, the simulation of hydrogen implantation requires the coupling of binary collision simulation and kinetic Monte Carlo simulation [84]. Since the simulation of the whole wafer is not feasible in reasonable time, a simplification with less computational effort is chosen. Instead of considering the whole structure, only a small volume is simulated. This volume, which in the following will be referred to as box, is "placed" at a certain depth and defects are recorded only in this region. Fig.5.5 shows a sketch of the simulation model. Implantation is simulated with IMSIL, point defects and ions coming to rest in the volume of the box are taken as input for the kLMC simulation.

An initial IMSIL run with 1000 ions gives the statistical properties of the interstitial and ion distribution, especially the lateral standard deviation σ , which is used to set the total size of the implantation area to $6\sigma * 6\sigma$ as shown in Fig.5.5. The area is divided into unit cells of the silicon lattice (lattice constant $a = 5.43\text{\AA}$). The necessary number of ions per cell (NIONS) is calculated to achieve the total implantation dose.

$$NIONS = dose \times (5,43 \times 10^{-10}m)^2 \quad (5.6)$$

The box is put below the middle of the area and the depth is chosen in regard to the defect and ion distribution (see Fig.5.5). For each unit cell the execution of IMSIL is repeated NIONS times. Since in IMSIL the ions start in the unit cell

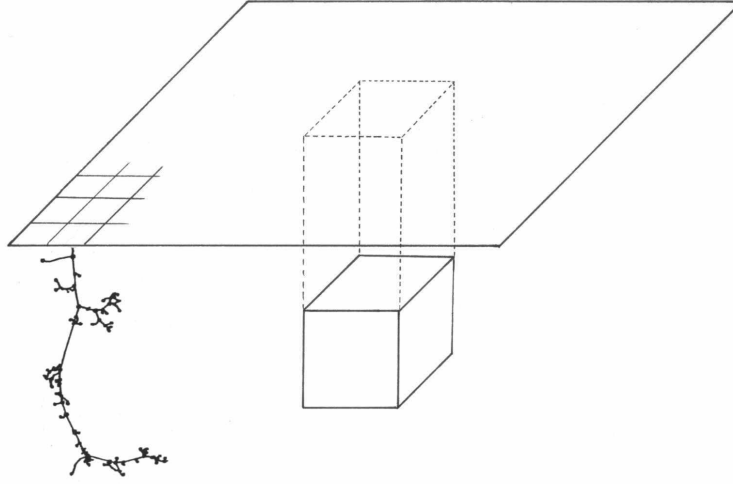


Figure 5.5: *Simulation of implantation*

around the origin the resulting cascade is shifted to the corresponding position of the unit cell and the defects inside the box are recorded, which means that the position and the defect species is stored in a defect file.

For the kLMC simulation the time between two implantations corresponds to the dose rate. The sequence of the defect files generated by the implantation step is chosen randomly to achieve a well-balanced implantation over the whole surface region. Defects resulting from an ion impact are repeatedly added to the box, using the defect files generated by IMSIL. Between two ion impacts the kLMC program simulates the thermally activated processes of the defects.

Chapter 6

Results

6.1 Initial damage and choice of simulation box

The simulation was done for hydrogen and deuterium implantation under exactly the same conditions given by the experiments on the isotope effect done by Moutanabbir *et al.* which is implantation at 5keV to a dose of $2 \times 10^{16} \text{cm}^{-2}$. Fig.6.1 and Fig.6.2 show the implantation depth profiles for hydrogen and deuterium obtained from IMSIL. It can be seen that deuterium implantation produces about twice as much damage as hydrogen implantation. Since deuterium ions have a longer implantation range compared to hydrogen ions, the deuterium profile is also broadened.

Corresponding to experimental investigations which showed platelet distributions centered around the mean projection range of hydrogen ions R_p [8], the simulation box was positioned at the depth of the maximum hydrogen/deuterium concentration obtained from the implantation depth profile. To confirm assumptions concerning defect evolution in the box and in regard to the investigations of the cutting location done by Höchbauer *et al.* [71] a second simulation was done with the box positioned at a depth corresponding to the maximum implantation damage.

The box had a size of 10x10x10nm in all cases, and the IMSIL runs were done with the parameters shown in Table 6.1, resulting in a total number of defects in these boxes as shown in Tab.6.2 and Tab.6.3.

6.2 Defect evolution

For the kinetic Monte Carlo simulation it was assumed that only vacancies, interstitials, and hydrogen atoms are mobile. Diffusion of all other species was not taken into account, because of either too high diffusion barrier or because of the fact, that larger defects are less likely to be mobile. The parameters for

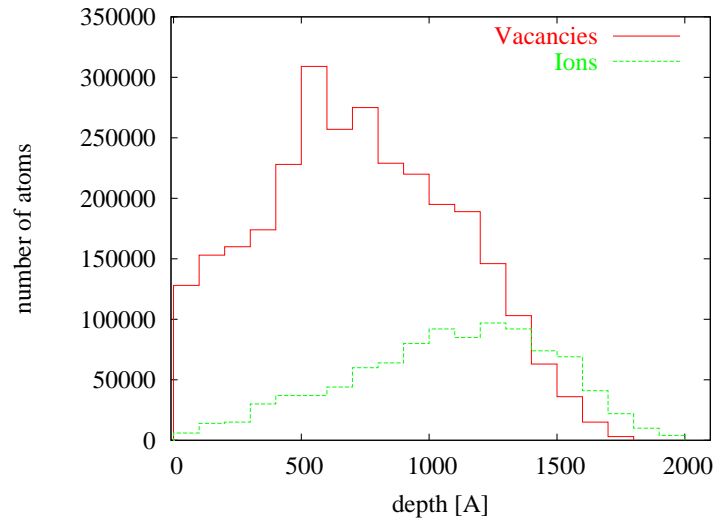


Figure 6.1: *Depth profile after simulation of hydrogen implantation at 5keV to a dose of $2 \times 10^{16} \text{cm}^{-2}$*

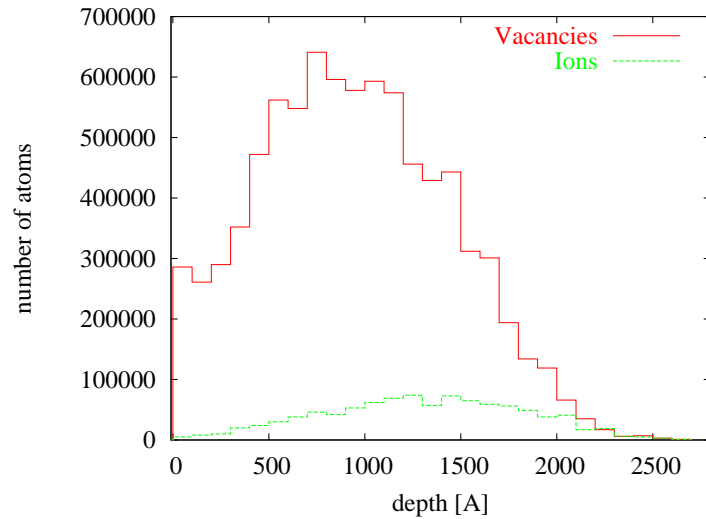


Figure 6.2: *Depth profile after simulation of deuterium implantation at 5keV to a dose of $2 \times 10^{16} \text{cm}^{-2}$*

the Monte Carlo simulation are shown in Tab.6.4.

It is well established that the diffusion coefficient of vacancies D_V is much higher than the diffusion coefficient of interstitials D_I and therefore these coefficients were not varied parameters. The hydrogen diffusion coefficient was considered uncertain compared to D_V and D_I . For this reason the simulation

	H	D
energy	5keV	5keV
dose	$2 * 10^{16}$	$2 * 10^{16}$
dose rate	$10\mu A/cm^2$	$10\mu A/cm^2$
NOINS	58	58
σ lateral(H)	366Å	441Å
number of unit cells	160000	230400

Table 6.1: *Implantation simulation parameters*

	H	D
Interstitials	2793	7726
Vacancies	2810	7740
Ions	1941	1431

Table 6.2: *Total number of defects generated by IMSIL in the box put into the hydrogen maximum*

	H	D
Interstitials	4898	11947
Vacancies	4884	11881
Ions	860	827

Table 6.3: *Total number of defects generated by IMSIL in the box put into the damage maximum*

Defect	Migration energy	Diffusion coefficient	Reference
Vacancy	0.4eV	$3 \times 10^{-13} \text{cm}^2/\text{s}$	[88],[87]
Interstitial	1eV	$1.5 \times 10^{-15} \text{cm}^2/\text{s}$	[88],[87]
Hydrogen/Deuterium	0.5eV	$1 \times 10^{-12} \text{cm}^2/\text{s}$	[29],[35]

Table 6.4: *Parameters for kinetic Monte Carlo Simulation*

of hydrogen and deuterium implantation was done for three different coefficients each. Unless otherwise noted the results discussed below are for a value of $1 \times 10^{-14} \text{cm}^{-2}$.

Since the most striking difference between hydrogen and deuterium implantation is the binding behavior the analysis of the simulation results was carried out in regard to this effect. Fig.6.3 and Fig.6.4 show the amount of hydrogen/deuterium bound to monovacancies and to multivacancies as a function of time with the box put into the hydrogen maximum. In the case of hydrogen implantation it can be seen that hydrogen atoms favor binding to monovacancies, whereas deuterium binds mostly to multivacancies. Fig.6.5 and Fig.6.6 show the same data for the box put into the maximum of implantation damage. Now both H and D are preferably bound to multivacancies, but deuterium to a larger

extent.

Table 6.5 compares the ratio of initial vacancy and hydrogen amount and the ratio of the number of hydrogen atoms bound to monovacancies and to multivacancies. It can be seen that for a smaller initial vacancy/hydrogen relation hydrogen binding to monovacancies is favored, whereas in the case of a bigger initial relation binding to multivacancies is dominant.

According to investigations done by Weldon *et al.* [11] and Moutanabbir *et al.* [5] VH_3 and VH_4 defects play an essential role in the nucleation of hydrogen platelets. The total number of VH_n defects for all four cases is shown in Tab. 6.6. A bigger amount of these two important defects can only be seen in the case of hydrogen implantation when the box is put into the hydrogen maximum.

As proposed by Martsinovich *et al.* [77] the evolution of $\text{H}_2^*/\text{D}_2^*$ might also be an important issue. Fig.6.7 and Fig.6.8 show the evolution of these defects as a function of time for the box put into the hydrogen maximum. After a time of approximately 50 seconds they evolve nearly linear and no big difference can be seen by comparing hydrogen and deuterium implantation. In addition, there are no bigger agglomerations of $\text{H}_2^*/\text{D}_2^*$ defects (data not shown here). The same data is shown in Fig.6.9 and Fig.6.10 for the box in the damage maximum. Here a somewhat larger number of H_2^* than D_2^* defects is found. However, their number is significantly lower than in the hydrogen/deuterium maximum, so that the difference is probably of minor relevance.

It has to be mentioned that an uncertainty concerning the formation of $\text{H}_2^*/\text{D}_2^*$ remains. As mentioned in Section 5.2.2 the H_2^* defect can be formed through Eq.5.4 or Eq.5.5. In kLMC the same reaction is possible in clusters. The H_2^* defect evolving out of these reaction are part of a defect cluster. So, the question is, whether these reactions can take place in a cluster in the same way as for an isolated interstitial/vacancy. Excluding this reaction for clusters would therefore decrease the number of H_2^* defects, mostly for the deuterium implantation, and increase the number of hydrogen atoms bound to multivacancies of the same amount.

Fig.6.11 shows the simulation results as a function of the hydrogen diffusion coefficient. The total number of hydrogen atoms bound to monovacancies and bound to multivacancies is compared to the number of deuterium atoms bound to monovacancies and to multivacancies. In all three cases the number of hydrogen atoms bound to monovacancies is higher than the number of hydrogen atoms bound to multivacancies. In contrast, the number of deuterium atoms bound to multivacancies is always higher than the number of deuterium atoms bound to monovacancies. This isotope effect is of nearly equal amount for the cases where $D_V < D_H$ ($10^{-12}\text{cm}^2/\text{s}$) and $D_V > D_H$ ($10^{-14}\text{cm}^2/\text{s}$), but is dramatically increased for the case where $D_V \gg D_H$ ($10^{-15}\text{cm}^2/\text{s}$). Moreover, it can be observed that the total number of hydrogen bound to vacancies is higher

than the amount of deuterium bound to vacancies.

	as-implanted			after annealing	
	V	H	V/H	H in V_mH_n	H in VH_n
Hydrogen _{hyd}	2810	1941	~1.4	~0.8	
Deuterium _{hyd}	7740	1431	~5.4	~2.2	
Hydrogen _{dam}	4884	860	~5.7	~1.54	
Deuterium _{dam}	11881	827	~14.4	~2.3	

Table 6.5: Ratio of initial vacancy/hydrogen amount and number of hydrogen in monovacancy-defects/multivacancy-defects after simulation; for deuterium replace H with D (subscript “hyd” denotes box in hydrogen maximum and “dam” denotes box in damage maximum)

	H_{hyd}	D_{hyd}	H_{dam}	D_{dam}
VH	16	40	26	34
VH ₂	27	15	13	9
VH ₃	19	9	4	1
VH ₄	54	3	5	1

Table 6.6: Total number of isolated VH defects for all four simulation cases (subscript “hyd” denotes box in hydrogen maximum and “dam” denotes box in damage maximum)

6.3 Discussion

The different binding behavior of hydrogen and deuterium shown in Fig.6.3 and Fig.6.4 can be explained by the different ratios of the number of vacancies and hydrogen/deuterium atoms. In a simplified picture only the motion of vacancies and hydrogen/deuterium atoms are considered. Moreover, it is neglected, that the annealing does not start at the end of the implantation, but during.

The evolution of hydrogenated vacancies can be divided into two steps. First the vacancies move and see other vacancies and hydrogen atoms. These vacancies can either bind to other vacancies forming cluster V_m or bind to hydrogen atoms $V+H \rightarrow VH+V \rightarrow V_2H+V \rightarrow \dots \rightarrow V_mH$. The larger the number of vacancies is, the larger m will be and the less isolated hydrogen atoms will remain.

As can be seen in Fig.6.1 and Fig.6.2 hydrogen produces less damage than deuterium. The motion of vacancies at the beginning of the simulation is illustrated in Fig.6.12. Since the number of vacancies is only 1.5 times higher than the number of hydrogen atoms, vacancy clusters and VH defects will form with approximately the same probability. Therefore m will be small and there will

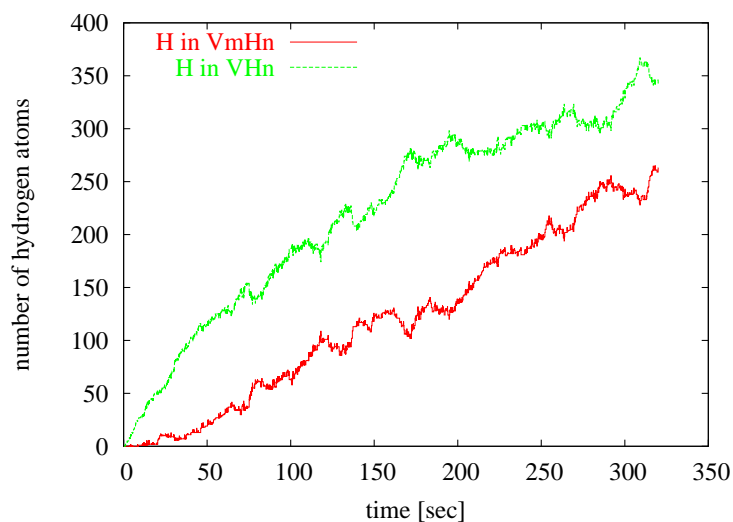


Figure 6.3: Comparison of hydrogen bound to monovacancies and to multivacancies for the box put into the hydrogen maximum

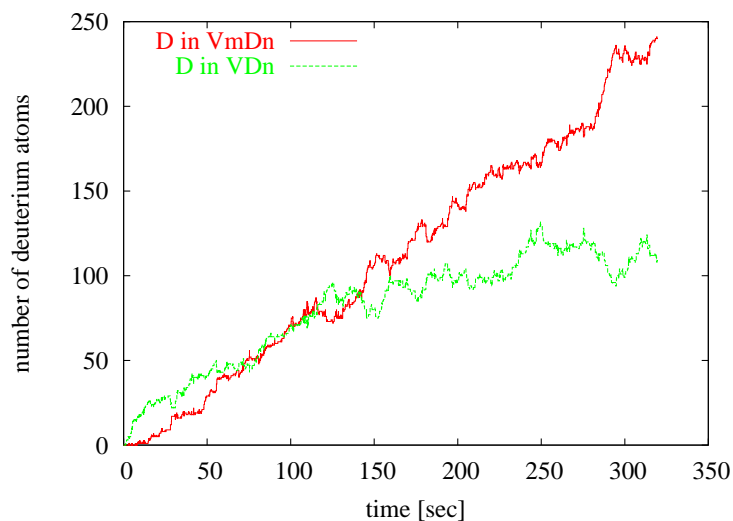


Figure 6.4: Comparison of deuterium bound to monovacancies and to multivacancies for the box put into the deuterium maximum

be a nearly equal amount of defects with $m=1$ and $m>1$. About half of the hydrogen atoms remain isolated after the vacancy motion step.

In the case of deuterium implantation the number of vacancies is more than 5 times higher than the number of deuterium atoms. Therefore m will be larger

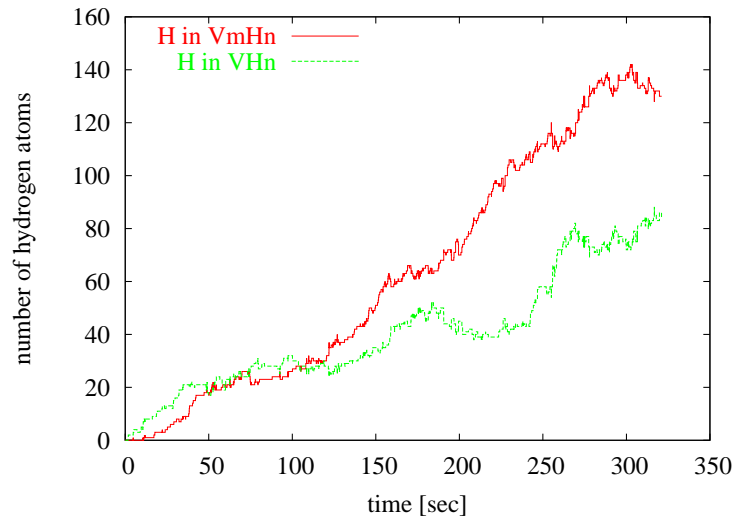


Figure 6.5: Comparison of hydrogen bound to monovacancies and to multivacancies for the box put into the damage maximum

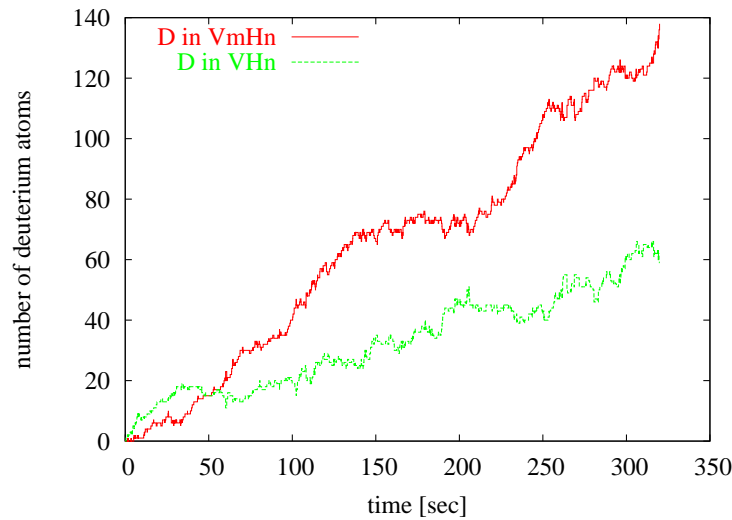


Figure 6.6: Comparison of deuterium bound to monovacancies and to multivacancies for the box put into the damage maximum

compared to hydrogen and there will be much more defects with $m > 1$ than defects with $m = 1$ and most of the deuterium atoms will be captured during the vacancy motion step (see Fig.6.13).

In the next step the remaining free hydrogen atoms start to move. The

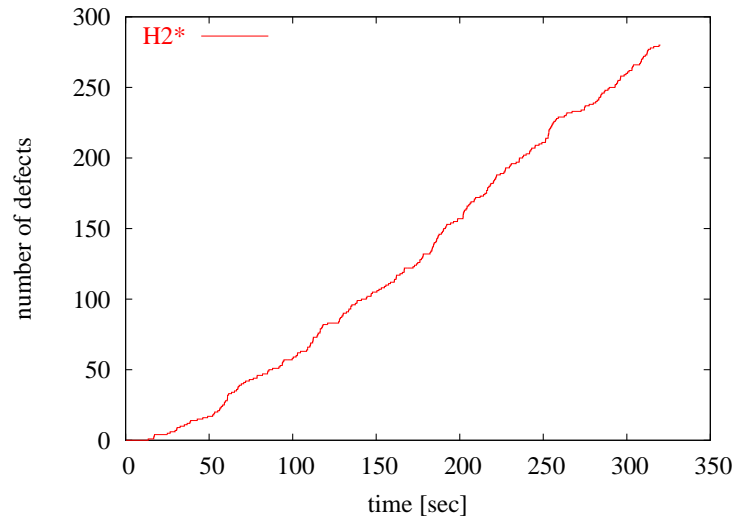


Figure 6.7: Evolution of H_2^* for the box put into hydrogen maximum

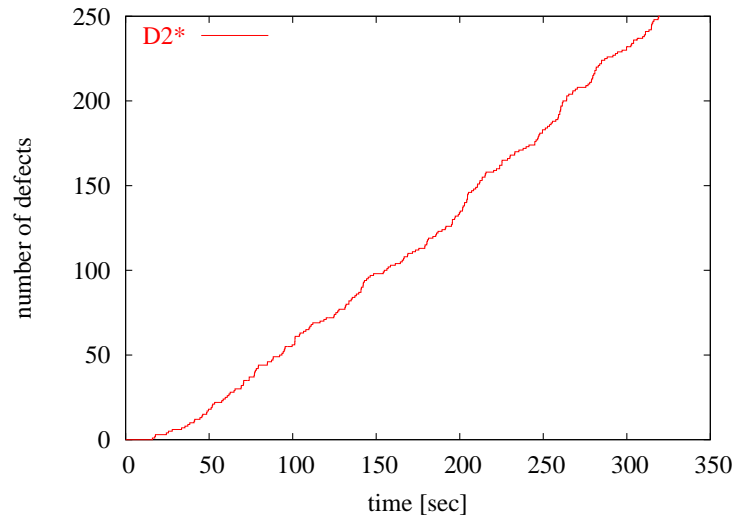


Figure 6.8: Evolution of D_2^* for the box put into deuterium maximum

hydrogen atoms can bind to the vacancy clusters forming V_mH , to the V_mH defects forming V_mH_2 and further on V_mH_n defects or to other hydrogen atoms. When the initial number of vacancies is small, then more hydrogen atoms remain after the vacancy motion step, which can move to VH defects in the next step and form VH_2 , VH_3 and VH_4 defects. If the initial number of vacancies is large, most of the hydrogen atoms get captured by the vacancies and there is little chance that VH_2 , VH_3 , and VH_4 defects are formed. This can be seen

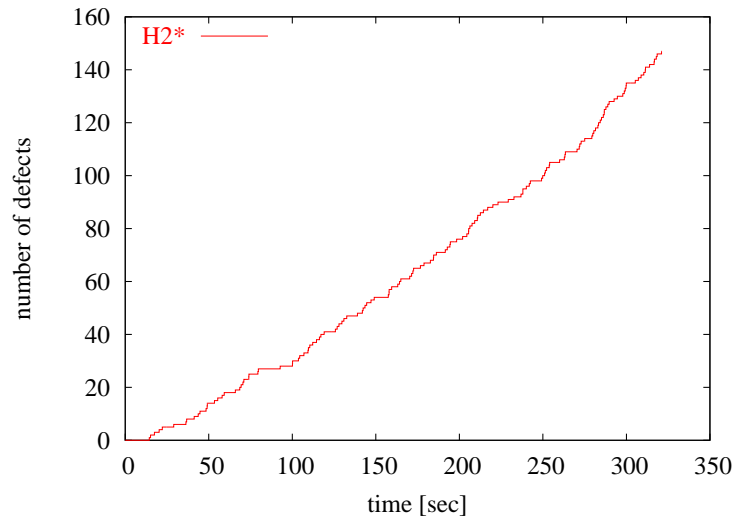


Figure 6.9: Evolution of H_2^* for the box put into damage maximum

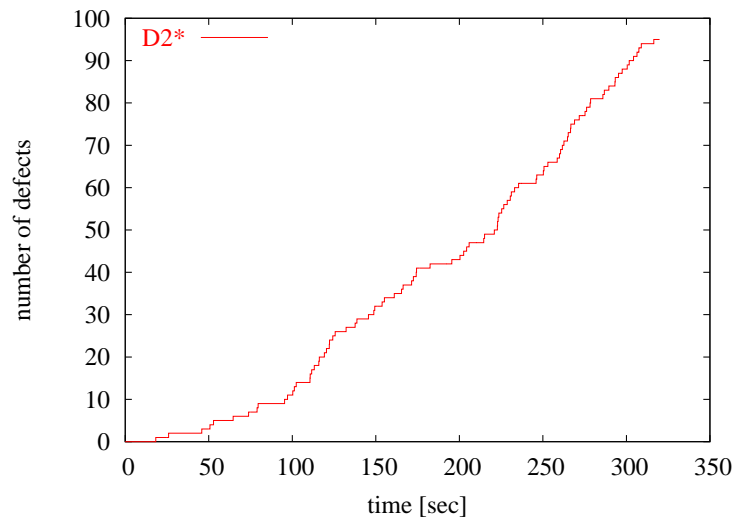


Figure 6.10: Evolution of D_2^* for the box put into damage maximum

in Tab.6.5 and Tab.6.6. In the case of hydrogen implantation, where half of the hydrogen atoms remain after vacancy motion VH_2 , VH_3 , and VH_4 evolve (see Fig.6.3). Only a small number of deuterium atoms remain in the case of deuterium implantation, which results in a very small number of VD_2 , VD_3 and VD_4 defects (see Fig.6.15).

This model is of course just a simplification of the implantation process,

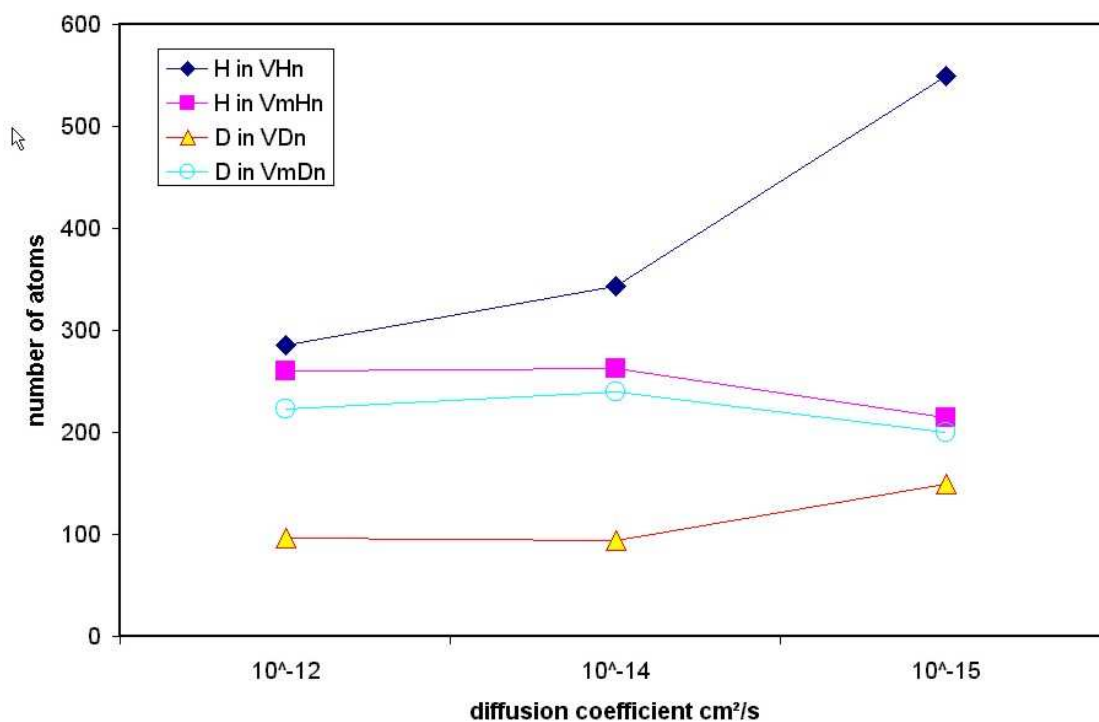


Figure 6.11: Isotope effect for different hydrogen diffusion coefficients

because it is assumed that diffusion does not take place until the whole dose is implanted. In reality diffusion is involved from the beginning of the implantation, which makes the explanation more complicated.

Since this behavior is due to the initial vacancy/hydrogen ratio the results for the box in the damage maximum shown (Fig.6.5 and Fig.6.6) are also quite reasonable. There the ratio of vacancies and hydrogen is comparable to that of vacancies and deuterium with the box set into the maximum of deuterium concentration. So it can be expected that hydrogen in the damage maximum (Fig.6.5) binds mostly to multivacancies as deuterium in the deuterium maximum (Fig.6.4), which is exactly what the result shows. But considering the hydrogen implantation profile (Fig.6.1) it can be expected that the average ratio of hydrogen and vacancies over the whole wafer depth will be similar to the ratio in the hydrogen maximum.

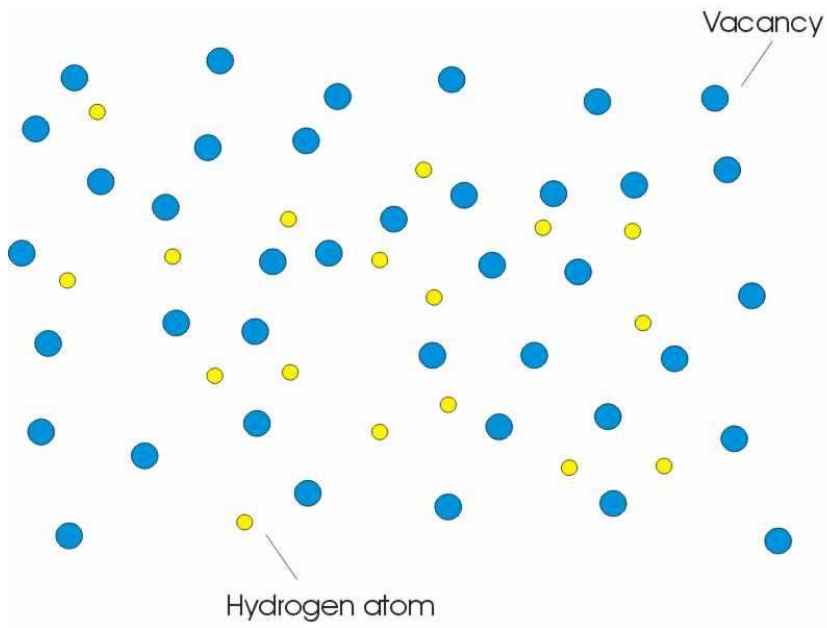


Figure 6.12: *Hydrogen implantation: before vacancy motion*

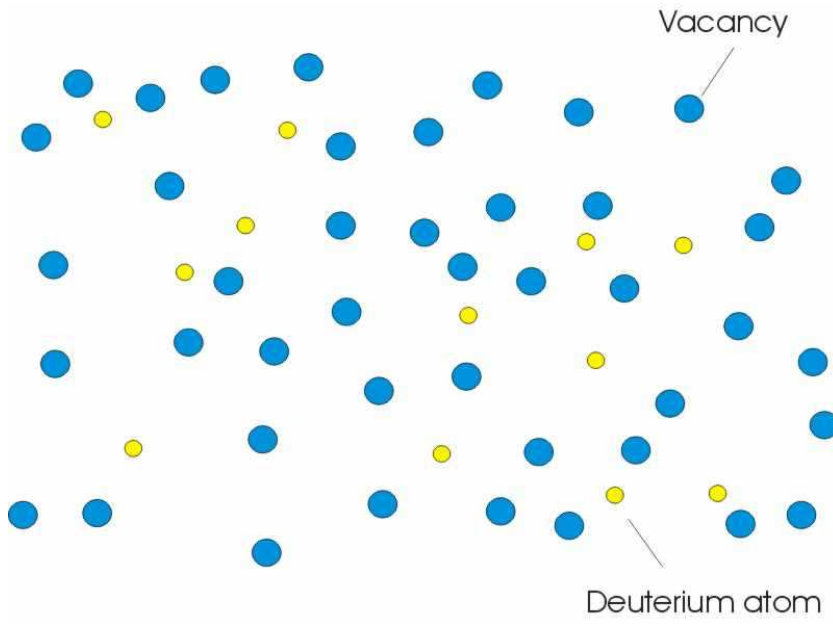


Figure 6.13: *Deuterium implantation: before vacancy motion*

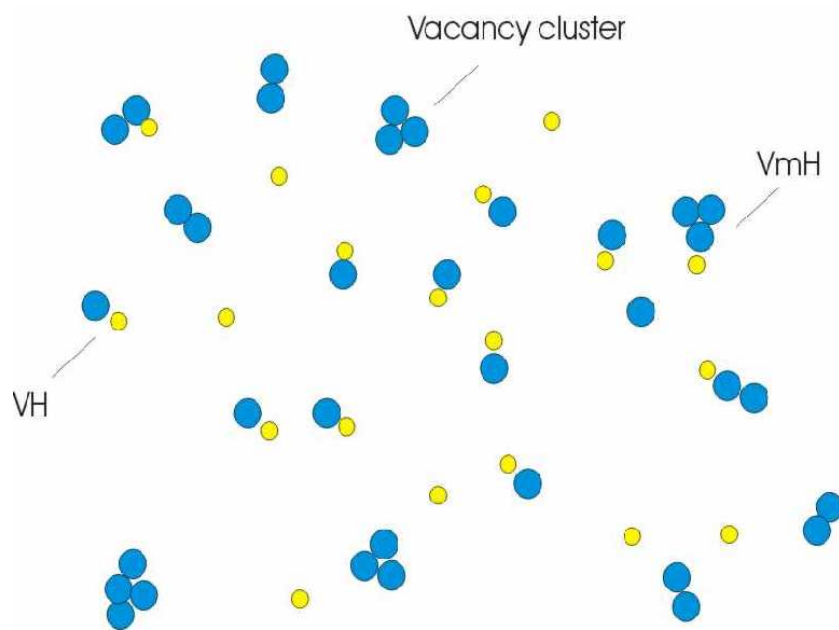


Figure 6.14: *Hydrogen implantation: after vacancy motion. A large number of H and VH exists*

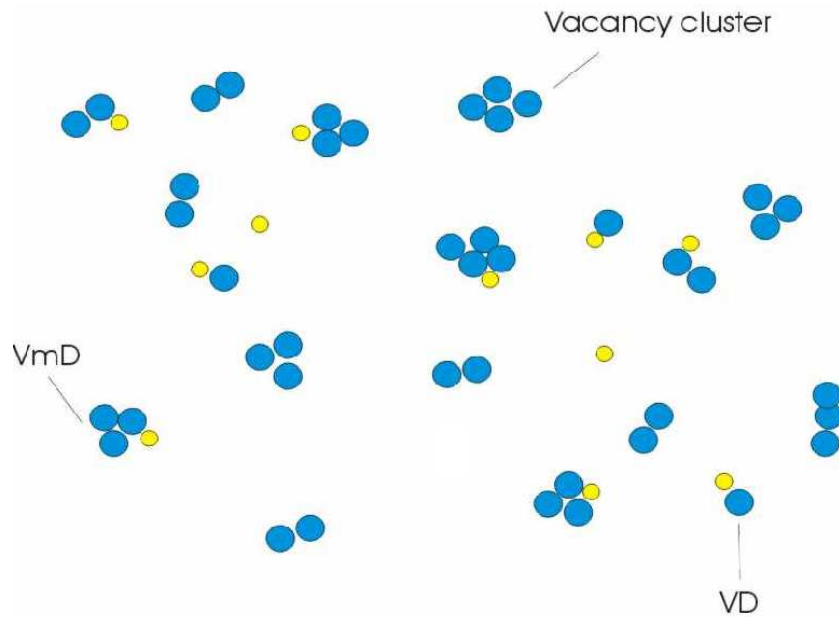


Figure 6.15: *Deuterium implantation: after vacancy motion. Only a small number of D and VD exists. Most D is bound to V_mD clusters with $m \geq 2$*

6.4 Conclusions

The goals for the simulation were the following:

- Calculate defect distribution and compare with experimental result
- Confirm or disprove the theory about the isotope effect of hydrogen induced blistering, which also includes the theory about VH_4 platelets
- Confirm or disprove the theory about H_2^* platelets

Simulation results showed that hydrogen binds preferably to monovacancies and deuterium binds mostly to multivacancies, when the simulation is done for a region around the maximum of the hydrogen distribution. Additionally, the monovacancy defects consist predominantly of VD for deuterium implantation and for the most part of VH_3 and VH_4 for the hydrogen implantation. This binding behavior can be explained by the different ratios of vacancies and hydrogen atoms. The bigger the damage is compared to the number of ions the more the binding to multivacancies is favored. Simulation of the maximum damage region does not show a different binding behavior, but is consistent with the proposed model. When regarding the whole wafer depth, it is to be expected that the average ratio of hydrogen and vacancies and of deuterium and vacancies will be the same as observed in the maximum of the hydrogen and the deuterium concentration. Moreover, this effect could be observed for all three hydrogen diffusion coefficient, which indicates that this coefficient is not a critical parameter for simulation.

An investigation of the resulting H_2^* and D_2^* defects showed no significant differences between hydrogen and deuterium also, bigger agglomerations of these defects could also not be found, which disagrees with the theory of H_2^* platelets.

In conclusion it can be reported that all of the simulation goals have been attained. The calculated defect distribution is similar to those obtained by experimental investigations. The theory concerning the isotope effect proposed by Moutanabbir *et al.* could be confirmed at the stage of initial defect distribution after implantation at room temperature. Therefore the theory of VH_4 could also be confirmed. Moreover, a simple model for the defect behavior during implantation at room temperature (Section 6.3) is proposed, which explains the difference between hydrogen-vacancy and deuterium-vacancy binding. Finally, the simulation results disagree with the theory of platelet nucleation based on H_2^* defects.

Chapter 7

Outlook

Despite the success of the simulations presented, additional simulations should be performed to confirm the results. First, due to intolerable computing time for the simulation of the whole wafer a restriction was made to a small area. Results showed that the isotope effect depends on the position of the box. Although it can be expected, that the isotope effect can be observed when considering the whole wafer depth, appropriate simulations have to be done to confirm this assumption.

Another interesting point would be the simulation of deuterium implantation to a dose sufficient to produce blisters. Since it would be reasonable that the reaction between ions and damage remains approximately the same, the total number of isolated VH defects, especially VH_3 and VH_4 , has to rise.

Consequently, for both hydrogen and deuterium implantation a dose exceeding the “blistering-window” should be simulated to investigate similarities of the defect behavior in the case of blister absence.

An important goal for future activities is the simulation of annealing above room temperature. For this purpose various energy parameters for binding have to be obtained by *ab initio* calculations.

Bibliography

- [1] S. Cristoloveanu and S.S. Li, *Electrical Characterization of Silicon-On-Insulator Materials and Devices*, Kluwer Academic Publishers (1995)
- [2] J.D. Plummer, M.D. Deal, and P.B. Griffin, *Silicon VLSI Technology*, Prentice Hall (2000)
- [3] G.K. Celler, S. Cristoloveanu, *J. Appl. Phys.* 93(9), 4955-4978 (2003)
- [4] C. Mazure, G.K. Celler, C. Maleville, and I. Cayrefourcq, *IEEE Int. Conf. Integrated Circuit Design and Technology* (2004)
- [5] O. Moutanabbir, B. Terrault, E. Shaffer, and G.G. Ross, *Mat. Res. Soc. Symp. Proc.* 792, R9.12 (2003)
- [6] O. Moutanabbir, A. Giguere, and B. Terreaux, *Appl. Phys. Lett.* 84(17), 3286-3288 (2004)
- [7] O. Moutanabbir and B. Terrault, *J. Chem. Phys.* 121(16), 7973-86 (2004)
- [8] B. Aspar, M. Bruel, H. Moriceau, C. Maleville, T. Poumeyrol, A.M. Papon, A. Claverie, G. Benassayag, A.J. Auberton-Herve, and T. Barge, *Microelectronic Engineering* 36, 233-240 (1997)
- [9] G.K. Celler, A.J. Auberton-Herve, B. Aspar, C. Lagahe-Blanchard, and C. Maleville, *Silicon-on-insulator by the Smart Cut™ process in Wafer bonding*, edited by M. Alexe, U. Gösele, Springer (2004)
- [10] M. Bruel, *Nucl. Instr. Meth. B*, 108, 313-319 (1996)
- [11] M.K. Weldon, V.E. Marsico, Y.J. Chabal, A. Agarwal, D.J. Eaglesham, J. Sapjeta, W.L. Brown, D.C. Jacobson, Y. Caudano, S.B. Christman, and E.E. Chaban, *J. Vac. Sci. Technol. B* 15(4), 1065-1073 (1997)
- [12] M. Bruel, *Electron. Lett.* 31, 1201-1202 (1995)
- [13] M. Bruel, *Mat. Res. Innovat.* 3, 9-13 (1999)
- [14] G. Hobler, K.K. Bourdelle, and T. Akatsu, *Nucl. Instr. Meth. B*, accepted for publication

- [15] H. Moriceau, F. Fournel, B. Aspar, B. Bataillou, A. Beaumont, C. Morales, A.M. Cartier, S. Pocas, C. Lagahe, E. Jalaguier, A. Soubie, B. Biasse, N. Soubie, S. Sartori, J.F. Michaud, F. Letertre, O. Rayssac, I. Cayrefourcq, C. Richtarch, N. Daval, C. Aulnette, T. Akutsu, B. Osternaud, B. Ghyselen, and C. Mazure, *J. Electron. Mat.* **32**, 829-835 (2003)
- [16] A. Agarwal, T.E. Haynes, V.C. Venezia, O.W. Holland, and D.J. Eaglesham, *Appl. Phys. Lett.* **72**(9),1086-88 (1998)
- [17] Q.Y. Tong, R. Scholz, U. Gösele, T.H. Lee, L.J. Huang, Y.L. Chao, and T.Y. Tan, *Appl. Phys. Lett.* **72**(1), 49-51 (1998)
- [18] C. Maleville, C. Mazure, *Solid State Electron.* **48**, 1055-1063 (2004)
- [19] L.Di Cioccio, Y. Le Tiec, F. Letertre, C. Jaussaud and M. Bruel, *Electron. Lett.* **32**(12) (1996)
- [20] I. Radu, I. Szafraniak, R. Scholz, M. Alexe, and U. Gösele, *J. Appl. Phys.* **94**(12), 7820-25 (2003)
- [21] E. Jalaguier, B. Aspar, S. Pocas, J.F. Michaud, A.M. Papon, and M. Bruel, *Int. Conf. Indium Phosphide and Related Materials*, 26-27 (1999)
- [22] B. Aspar, E. Jalaguier, A. Mas, C. Locatelli, O. Rayssac, H. Moriceau, S. Pocas, A.M. Papon, J.F. Michaud, and M. Bruel, *Electron. Lett.* **35** 1024-1025 (1999)
- [23] C. Maleville, T. Barge, B. Ghyselen, and A.J. Auberton, *IEEE Intl. SOI Conf.*, Oct. 2000
- [24] B. Aspar, M. Bruel, M. Zussy, and A.M. Cartier, *Electron. Lett.* **32**, 1985-1986 (1996)
- [25] S.K. Estreicher, M.A. Roberson, and D.J.M. Maric, *Phys. Rev. B* **50**(23), 17018-27 (1994)
- [26] C.G. Van de Walle and R.A. Street, *Phys. Rev. B* **49**(20), 14766-69 (1994)
- [27] C. Herring, N.M. Johnson, and C.G. Van de Walle, *Phys. Rev. B* **64**, 125209 (2001)
- [28] P. Deak, L.C. Snyder, and J.W. Corbett, *Phys. Rev. B* **43**(5), 4545-4547 (1991)
- [29] P. Deak, L.C. Snyder, and J.W. Corbett, *Phys. Rev. B* **37**(12), 6877-6892 (1988)
- [30] N.M. Johnson and C. Herring, *Phys. Rev. B* **38**(2), 1581 (1988)
- [31] N.M. Johnson and C. Herring, *Phys. Rev. B* **46**(12), 15554 (1992)

- [32] C.G. Van de Walle, Y. Bar-Yam, and S.T. Pantelides, *Phys. Rev. Lett.* 60, 2761 (1988)
- [33] C.G. Van de Walle, P.J.H. Denteneer, Y. Bar-Yam, and S.T. Pantelides, *Phys. Rev. B*, 39(15) 10791-10807 (1989)
- [34] R.H. Doremus, *Mat. Res. Innovat.* 4, 49-59 (2000)
- [35] S. Bedard and L.J. Lewis, *Phys. Rev. B* 61(5), 9895-9898 (2000)
- [36] E. Elinor Chen, M. Stavola, W. Beall Fowler, and P. Walters, *Phys. Rev. Lett.* 88(10), 105507 (2002)
- [37] C.G. Van de Walle, *Phys. Rev. Lett.* 80(10), 2177-2180 (1998)
- [38] R.E. Pritchard, M.J. Ashwin, J.H. Tucker, and R.C. Newman, *Phys. Rev B* 57(24), 15048 (1998)
- [39] W. Beall Fowler, P. Walters, and M. Stavola, *Phys. Rev. B* 66, 75216 (2002)
- [40] B. Hourahine, R. Jones, S. Ödberg, and P.R. Briddon, *Mat. Sci. Eng. B* 58, 24-25 (1999)
- [41] R.E. Pritchard, M.J. Ashwin, R.C. Newman, J.H. Tucker, *Mat. Sci. Eng. B* 58, 1-5 (1999)
- [42] A.W.R. Leitch, J. Weber, and V. Alex, *Mat. Sci. Eng. B* 58, 6-12 (1999)
- [43] N. Fukata, S. Sasaki, K. Murakami, K. Ishioka, K.G. Nakamura, M. Kitajima, S. Fujimura, J. Kikuchi, and H. Haneda, *Phys. Rev. B* 56(11), 6642-6647 (1997)
- [44] S.K. Estreicher, K. Wells, P.A. Fedders, and P. Ordejon, *J. Phys. Condens. Matter* 13, 6271 (2001)
- [45] M. Stavola, E. Elinor Chen, W. Beall Fowler, G. Alvin Shi, *Physica B* 340-342, 58-66 (2003)
- [46] K.J. Chang and D.J. Chadi, *Phys. Rev. Lett.* 62(8), 937-940 (1989)
- [47] K.J. Chang and D.J. Chadi, *Phys. Rev. B* 40(17) (1989)
- [48] N.M. Johnson and C. Herring, *Phys. Rev. B* 43(17), 14297-14300 (1991)
- [49] J.D. Holbeck, B. Bech Nielsen, R. Jones, P. Sitch, and S. dberg, *Phys. Rev. Lett.* 71(6), 875-878 (1993)
- [50] S.K. Estreicher, J.L. Hasting, P.A. Fedders, *Phys. Rev. Lett.* 82(4), 815-818 (1999)
- [51] Y.K. Park, S.K. Estreicher, C.W. Myles, and P.A. Fedders, *Phys. Rev. B* 52(3), 1718-1723 (1995)

- [52] J.M. Pruneda, J. Junquera, J. Ferrer, P. Ordejon, and S.K Estreicher, *Physica B* 308-310, 147-150 (2001)
- [53] M. Budde, B. Bech Nielsen, P.R. Briddon, S. Ödberg, and S.J. Breuer, *Phys. Rev. B* 57(8), 4397-4412 (1998)
- [54] E.V. Lavrov, J. Weber, L. Huang, and B. Bech Nielsen, *Phys. Rev. B* 64, 35204 (2001)
- [55] B. Bech Nielsen, J. Olajos, and H.G. Grimmeiss, *Phys. Rev. B* 39(5), 3330-3336 (1989)
- [56] B. Bech Nielsen, L. Hoffmann, and M. Budde, *Mat. Sci. Eng. B* 36, 259-263 (1996)
- [57] S.K. Estreicher, J.L. Hastings, and P.A. Fedders, *Mat. Sci. Eng. B* 58, 31-35 (1999)
- [58] S.B. Zhang and H.M. Branz, *Phys. Rev. Lett.* 87(10), 105503 (2001)
- [59] M. Gharaibeh, S.K. Estreicher, P.A. Fedders, and P. Ordejon, *Phys. Rev. B* 64, 235211 (2001)
- [60] B.L. Sopori, X. Deng, J.P. Benner, A. Rohatgi, P. Sana, S.K. Estreicher, Y.K. Park, and M.A. Roberson, *Sol. Energ. Sol. Cel.* 41/42, 159-169 (1996)
- [61] N.M. Johnson, F.A. Ponce, R.A. Street, and R.J. Nemanich, *Phys. Rev. B*, 35(8), 4166-4169 (1987)
- [62] J. Grisolia, G. Ben Assayag, A. Claverie, B. Aspar, C. Lagahe, and L. Laanab, *Appl. Phys. Lett* 76(7), 852-854 (2000)
- [63] L.B. Freund, *Appl. Phys. Lett.* 70(26), 3519-3521 (1997)
- [64] C.M. Varma, *Appl. Phys. Lett.* 71(24), 3519-3521 (1997)
- [65] F. Yang, *J. Appl. Phys.* 94(3), 1454-1457 (2003)
- [66] Q.Y Tong, K. Gutjahr, S. Hopfe, U. Gsele, and T.H. Lee, *Appl. Phys Lett.* 70(11), 1390-92 (1997)
- [67] L.J. Huang, Q.Y. Tong, Y.L. Chao, T.H. Lee, T. Martini, and U. Gsele, *Appl. Phys. Lett.* 74(7),982-984 (1999)
- [68] K. Mitani and U. Gösele, *Appl. Phys. A* 54, 543 (1992)
- [69] Y. Zheng, S.S. Lau, T. Hchbauer, A.Misra, R. Verda, X.M. He, M. Nastasi, and J.W. Mayer, *J. Appl. Phys.* 89(5), 2972-2978 (2001)
- [70] B. Aspar, C. Lagahe, H. Moriceau, A. Soubie, and M. Bruel, *Proc. IEEE Int. SOI Conf.* 1998

- [71] T. Höchbauer, A. Misra, R. Verda, M. Nastasi, J.W. Mayer, Y. Zheng, and S.S. Lau, *Phil. Mag. B* 80(11), 1921-1931 (2000)
- [72] T. Höchbauer, A. Misra, R. Verda, Y. Zheng, S.S. Lau, J.W. Mayer, and M. Nastasi, *Nucl. Instrum. Meth. B*, 175-177, 169-175 (2001)
- [73] T.Höchbauer, A. Misra, M. Nastasi, and J.W. Mayer, *J. Appl. Phys.* 89(11), 5980-5990 (2001)
- [74] T. Höchbauer, M. Nastasi, R.D. Verda, A. Misra, K. Henttinen, I. Suni, S.S. Lau, and J.W. Mayer, *Nucl. Instr. Meth. B* 190, 592-597 (2002)
- [75] S.B. Zhang and W.B. Jackson, *Phys. Rev. B*, 43(14), 12142-45 (1991)
- [76] Y.S. Kim and K.J. Chang, *Phys. Rev. Lett.* 86(9),1773-1776 (2001)
- [77] N. Martsinovich, M.I. Heggie, and C.P. Ewels, *J. Phys. Condens. Matter* 15, 2815-2824 (2003)
- [78] N. Martsinovich, A.L. Rosa, M.I. Heggie, C.P. Ewels, and P.R. Briddon, *Physica B* 340-342, 654-658 (2003)
- [79] F.A. Reboredo, M. Ferconi, and S.T. Pantelides, *Phys. Rev. Lett.* 82(24), 4870-4873 (1999)
- [80] G. Hobler, *IMSIL manual* (2004)
- [81] G. Hobler, *Nucl. Instr. Meth. B* 96, 155-162 (1995)
- [82] G. Hobler, *Skriptum zur Vorlesung "Physikalische Prozessmodellierung"*
- [83] G. Otto, G. Hobler, *Mat. Res. Soc. Symp. Proc.* 792, R6.5.1-6 (2003)
- [84] G. Hobler, G. Otto, D. Kovač, L. Palmethofer, K. Mayerhofer, K. Piplits, *Nucl. Instr. Meth. B*, accepted for publication (2004)
- [85] M. Jaraiz, E. Rubio, P. Castrillo, L. Pelaz, L. Bailon, J. Barbolla, G.H. Gilmer, and C.S. Rafferty, *Mat. Sci. Sem. Proc.* 1, 237 (1998)
- [86] M. Jaraiz, P. Castrillo, P. Pinacho, I. Martin-Bragado, and J. Barbolla, *SISPAD Conference* 2001
- [87] S. Libertino, S. Coffa, C. Spinella, A. La Magna, V. Privitera, *Nucl. Instr. Meth. B* 178, 25 (2001)
- [88] L. Pelaz, M. Jaraiz, G.H. Gilmer, H.J. Gossmann, C.S. Rafferty, D.J. Eaglesham, J.M. Poate, *Appl. Phys. Lett.* 70(17), 2285-7 (1997)

Publications

T. Zahel, G. Otto, and G. Hobler, Atomistic Simulation of Hydrogen Implantation for SOI Wafer Production, EUROSIOI Workshop 2005, Granada, Spain, Jan. 19-21, 2005, accepted for presentation

T. Zahel, G. Otto, and G. Hobler, Atomistic Simulation of the Isotope Effect on Defect Formation in H/D-implanted Si, 12th Int. Symposium on SOI Device Technology, 207th ECS meeting 2005, Quebec, Canada, May 15-20, 2005, submitted

List of Figures

1.1	CMOS transistor built in (a) Si-bulk and (b) SOI technology (from [1])	8
2.1	Optical microscopy image of silicon implanted to a dose of $1 \times 10^{17} \text{H/cm}^2$ and annealing to 475°C (from [11])	12
2.2	AFM image of the sample shown in 2.1 (from [11])	12
2.3	Smart Cut™ process steps (from [9])	13
2.4	TEM of a SOI structure obtained by smart-cut (from [13])	14
3.1	AFM images of silicon surfaces implanted with 5keV hydrogen and annealing up to 650°C (a) $2 \times 10^{16} \text{cm}^{-2}$ (b) $4 \times 10^{16} \text{cm}^{-2}$ (c) $6 \times 10^{16} \text{cm}^{-2}$ (from [5])	18
3.2	Blister-covered area as a function of total fluence of H and/or D implanted at 5keV (from [6])	19
3.3	Blister-covered area as a function of H fluence at 2, 5, and 10keV (from [6])	19
3.4	Hydrogen thermal desorption spectra of Si implanted at 5keV with (a) $2 \times 10^{16} \text{cm}^{-2}$ (b) $6 \times 10^{16} \text{cm}^{-2}$ (from [6])	21
3.5	Thermal desorption spectra of Si implanted at 5keV with (a) $2 \times 10^{16} \text{Hcm}^{-2}$ (b) $2 \times 10^{16} \text{Dcm}^{-2}$ (from [5])	21
3.6	Si-H/D stretch mode regions of the Raman Scattering spectra obtained after implantation with $2 \times 10^{16} \text{cm}^{-2}$ (a) H implantation (b) D implantation (from [7])	23
3.7	Temperature evolution of the Si-H stretch modes of Si implanted with $2 \times 10^{16} \text{Hcm}^{-2}$ (from [7])	24
3.8	Temperature evolution of the Si-H stretch modes of Si implanted with $2 \times 10^{16} \text{Dcm}^{-2}$ (from [7])	25
3.9	Temperature evolution of the Si-H stretch modes of Si implanted with $6 \times 10^{16} \text{Dcm}^{-2}$ (from [7])	26
4.1	H_2^* defect (from [49])	28
4.2	TEM view of a microcrack distribution after hydrogen implantation at room temperature (from [9])	32

4.3	Evolution of the mean diameter, the density and the average volume of platelets (from [62])	33
4.4	TEM view of a macrocrack after annealing (from [9])	34
4.5	TEM view of platelet distributions for different wafer orientations after hydrogen implantation (from [69])	36
4.6	Transformation of hydrogen during annealing (from [11])	37
4.7	Location of the H-induced splitting (from [72])	38
4.8	TEM view of “popped” blisters (from [74])	39
4.9	IR spectra of the Si-H stretching modes of hydrogen implanted Si at a dose of $2 \times 10^{16} \text{ cm}^{-2}$ at (i) room temperature and after annealing to (ii) 300°C (iii) 425°C (iv) 500°C (v) 550°C (vi) 650°C (from [11])	41
4.10	IR spectra of the Si-H stretching modes of hydrogen implanted Si at a dose of $6 \times 10^{16} \text{ cm}^{-2}$ at (i) room temperature and after annealing to (ii) 300°C (iii) 425°C (iv) 500°C (v) 550°C (vi) 650°C (from [11])	42
4.11	Activation energy for layer splitting (from [70])	45
4.12	Simple platelet model (from [63])	46
4.13	Model for hydrogen platelets (from [64])	48
4.14	Activation energies for blistering/splitting (from [66])	48
4.15	Onset-time for blistering (from [67])	49
4.16	Critical size vs. implant depth (from [67])	49
4.17	Possible structures for (111) hydrogen platelets (from [58])	52
4.18	Structures for mid-size and larger platelets (from [77])	53
4.19	Structures for finite number of hydrogen atoms (from [78])	54
5.1	Binary Collision (from [82])	59
5.2	kMC concept: (a) shows a TEM view of a $\{311\}$ defect, circles in (b) and (c) represent the defect atoms simulated by Monte Carlo (from [86])	62
5.3	Energy parameters for kinetic Monte Carlo simulation (from [86])	63
5.4	Simulation flow of kinetic Monte Carlo simulation	63
5.5	Simulation of implantation	65
6.1	Depth profile after simulation of hydrogen implantation at 5 keV to a dose of $2 \times 10^{16} \text{ cm}^{-2}$	68
6.2	Depth profile after simulation of deuterium implantation at 5 keV to a dose of $2 \times 10^{16} \text{ cm}^{-2}$	68
6.3	Comparison of hydrogen bound to monovacancies and to multivacancies for the box put into the hydrogen maximum	72
6.4	Comparison of deuterium bound to monovacancies and to multivacancies for the box put into the deuterium maximum	72
6.5	Comparison of hydrogen bound to monovacancies and to multivacancies for the box put into the damage maximum	73
6.6	Comparison of deuterium bound to monovacancies and to multivacancies for the box put into the damage maximum	73

6.7	Evolution of H_2^* for the box put into hydrogen maximum	74
6.8	Evolution of D_2^* for the box put into deuterium maximum	74
6.9	Evolution of H_2^* for the box put into damage maximum	75
6.10	Evolution of D_2^* for the box put into damage maximum	75
6.11	Isotope effect for different hydrogen diffusion coefficients	76
6.12	Hydrogen implantation: before vacancy motion	77
6.13	Deuterium implantation: before vacancy motion	77
6.14	Hydrogen implantation: after vacancy motion. A large number of H and VH exists	78
6.15	Deuterium implantation: after vacancy motion. Only a small number of D and VD exists. Most D is bound to V_mD clusters with $m \geq 2$	78

List of Tables

1.1	<i>SOITEC SOI roadmap (from [4])</i>	9
4.1	<i>Spectral features before annealing (from [11])</i>	43
4.2	<i>Spectral features upon annealing up to 650°C (from [11])</i>	43
5.1	<i>Possible defects for the simulation of hydrogen implantation</i>	64
6.1	<i>Implantation simulation parameters</i>	69
6.2	<i>Total number of defects generated by IMSIL in the box put into the hydrogen maximum</i>	69
6.3	<i>Total number of defects generated by IMSIL in the box put into the damage maximum</i>	69
6.4	<i>Parameters for kinetic Monte Carlo Simulation</i>	69
6.5	<i>Ratio of initial vacancy/hydrogen amount and number of hydrogen in monovacancy-defects/multivacancy-defects after simulation; for deuterium replace H with D (subscript “hyd” denotes box in hydrogen maximum and “dam” denotes box in damage maximum)</i>	71
6.6	<i>Total number of isolated VH defects for all four simulation cases (subscript “hyd” denotes box in hydrogen maximum and “dam” denotes box in damage maximum)</i>	71